DYNAMIC RUPTURES OF THE 2016 M_L 6.6 MEINONG EARTHQUAKE AND POTENTIAL GROUND MOTION FROM SCENARIO EARTHQUAKES ON THE CHINSHAN-SHANQIAO FAULT, TAIWAN, WITH 3D VELOCITY STRUCTURES

A Dissertation

by

LEIYIN JIAO

Submitted to the Office of Graduate and Professional Studies of
Texas A&M University
in partial fulfillment of the requirements for the degree of

DOCTOR OF PHILOSOPHY

Chair of Committee,	Benchun Duan
Committee Members,	Mark Everett
	Hiroko Kitajima
	Luciana Barroso
	Richard Gibson
Head of Department,	Julie Newman

December 2019

Major Subject: Geophysics

ABSTRACT

Dynamic ruptures of the 2016 Meinong earthquake and potential ground motion induced by earthquake scenarios on the geometrically complex Chinshan-Shanqiao faults in Taiwan have been modeled. Realistic 3D velocity structures have been incorporated for Chinshan-Shanqiao earthquake scenarios. In the first study, we use dynamic ruptures to reproduce slip distribution, rupture process and moment rate history from Meinong earthquake kinematic inversions to understand the mechanics that causes the complex rupture details. The earthquake occurs on a buried and shallow dipping fault with dominant left-lateral strike slip with limited amount of thrusting. By trial-and-error, we find in our best fit model two asperities with sizes of 15 by 8 km and of 10 by 6 km that dominate the moment release. The average stress drops in the two asperities are 5.0 and 3.5 MPa, respectively. The whole rupture region is 25 by 25 km. Except for asperities, the region near the hypocenter has a very low 0.75 MPa stress drop. The magnitude of the best model is M_w 6.63 and the maximum slip is 1.4 m, close to M_w 6.52 and 1.2 m from inversions. We apply a uniform velocity structure to simulate ground motions and find the simulated peak ground velocities match the seismograms on rock sites in 0-0.5 Hz. Inside low-velocity sedimentary Tainan basin, simulated peak ground velocities also match the recorded vertical peak ground velocities. However, the horizontal peak ground velocities are less than those from records. Therefore, we conclude that the uniform velocity structure works well for the rock sites but 3D velocity structure is important to generate the large horizontal ground motions recorded in the Tainan basin during the earthquake.

In the second study, we simulate potential ground motion from scenario earthquakes on the geometrically complex Chinshan-Shanchiao faults. Realistic 3D velocity structure including the low-velocity sedimentary basin is included. The Chinshan-Shanchiao fault is the west bound to the Taipei basin in northern Taiwan. It is a highly active normal fault with left strike-slip components and is speculated to host a potential future earthquake with a magnitude over 7.0. By comparing models with uniform and 3D realistic velocity structure, we find that seismic energy can be trapped in the Taipei basin. Stations inside and on the edge of the basin show amplified peak ground acceleration and prolongated waveforms. The kink fault geometry also contributes to amplification of ground motion. The peak ground acceleration and peak ground velocity of the stations in the west of the basin are larger than those in the east of the basin. This effect appears to be related to the shape of the basin.

ACKNOWLEDGEMENTS

I would like to specially thank my committee chair, Dr. Benchun Duan, for supporting and encouraging me through the most difficult time in my study and life. Also, I would like to thank my friends and colleagues Dunyu Liu, who helped me with my research, Guangjian Xu, Szu-Ting Kuo, Bin Luo, Zhenhua He and others, who shared the most wonderful experience with me at Texas A&M University.

I would like to thank my committee members, Drs. Mark Everett, Hiroko Kitajima, Richard Gibson, and Luciana Barroso for their guidance and support throughout the course of this research.

Finally, I would like to thank my husband who has always been there for me and helped me to become a better individual and my parents who always let me chase my dreams whatever they may be.

CONTRIBUTORS AND FUNDING SOURCES

This work was supervised by a dissertation committee including Drs. Benchun Duan [advisor], Mark Everett, Hiroko Kitajima, and Richard Gibson of the Department of Geology and Geophysics, and Dr. Luciana Barroso of the Department of Zachry Department of Civil & Environmental Engineering. This work was supported by China Scholarship Council and partially supported by National Science Foundation through grant EAR-1254573. We appreciate Texas A&M High Performance Research Computing (https://hprc.tamu.edu) for providing the computing resources used in this study.

TABLE OF CONTENTS

Page

LIST OF FIGURES

Page

LIST OF TABLES

Page

1. INTRODUCTION AND OVERVIEW

The dissertation is devoted to applications of spontaneous rupture models and parallel finite element methods to explore source processes and to evaluate ground shaking hazard from earthquakes in Taiwan.

Taiwan is located where Philippine Sea plate and Eurasian plate collide with each other. The Philippine Sea plate moves northwestwards at a speed of 8.2 cm yr^{-1} [Yu *et al*. 1997]. The collision accounts for the high seismicity in Taiwan. In the past hundreds of years, a lot of earthquakes in or near the Taiwan island lead to huge causalities and property loss. For example, the M_w 7.1 Hsinchu-Taichung earthquake struck central Taiwan in 1935 and it took about 3000 lives and destroyed 17000 houses [Lin *et al*., 2013; Hsu, 1971]. The M_w 7.6 1999 Chi-Chi earthquake is the largest earthquake on the Taiwan island in the twentieth century. It caused 2470 death, 11,305 people injured, and more than 100,000 structures destroyed in densely populated central and western Taiwan [Shin and Teng, 2001]. There was also a sequence of earthquakes in the Hualien area in the northeastern Taiwan since 1920s which caused huge damage.

The fault systems are complex in Taiwan. In 2012, the Central Geological Survey (CGS) of Ministry of Economic Affairs in Taiwan reports at least 33 active faults (Figure 1.1) with documented surface ruptures. Some faults are associated with previous large earthquakes, like that the 1935 Hsinchu-Taichung earthquake occurred on the Shihtan fault (No. 5) and the Tuntzuchiao fault (No. 9) [Lin *et al*., 2013]. The 1999 Chi-Chi earthquake happened on the Chelungpu fault (No. 11) and the Tamaopu-Shuangtung fault

(No. 12). Parts of the Chinshan-Shanchiao fault system (No. 1) might have host the 1867 Keelung earthquake [Tsai, 1986]. According to Chang *et al*. [2016], the fault slip rate deficit of the Shanchiao fault system is between 0.7 and 1.5mm/yr and it has a potential to host a M_w 6.3-7.4 earthquake in the next fifty years. The fault is also classified as high-risk active faults by the risk assessment of Wang *et al*. [2013]. In addition, the Shanchiao fault cuts right through the west edge of the Taipei basin, where the Taipei city is located. It is also close to two nuclear power plants: the Chishan nuclear power plant 7 km away and the Kuosheng plant 5 km away. Therefore, it is necessary to assess seismic hazard from potential earthquake scenarios with magnitudes over 7.0 on the Shanchiao-Chishan fault [Wang, 2008; Lai, 2010; Huang *et al*., 2007].

In terms of ground shaking, the Taipei basin is a triangular-shaped alluvium basin filled with the Quaternary unconsolidated sediments overlying the Tertiary basement. Amplification and prolongation of sedimentary basin-induced waves could enlarge significantly the peak ground velocity [Hough *et al*., 1990; Olsen *et al*., 2009]. Therefore, we simulate scenario earthquakes on the geometrically complex Chinshan-Shanchiao fault with 3D basin velocity structures to assess ground shaking hazard near Taipei. The results show that the rupture seems to be facilitated by the bends along the strike of the normal fault. The rupture propagation and ground motions are sensitive to the choice of physical parameters R and S that are discussed in later chapter. Also, ground motions are affected significantly by the amplification effect and the shape of Taipei basin.

There are many buried or hidden faults in Taiwan that led to huge damage. For example, the Shihtan and Tuntzuchiao faults, which host the 1935 Hsinchu-Taichung

earthquake, are partially exposed to the surface. On the other hand, Taiwan is under compressional stress condition where the Philippine sea plate and the Eurasian plate collide with each other, therefore most of the faults are thrust faults. In Figure 1.1, among the 33 active faults, only No. 1 Shanchiao fault is normal fault; No. 9, 14, 15, 19 are right lateral strike slip faults with thrust components; No. 21, 26, 27, 28, 30, 31 are left lateral strike slip faults with thrust components; The rest 22 faults are pure thrust faults. The 2016 M_L 6.6 Meinong earthquake occurred on a blind low dipping angle thrust fault with dominant left-lateral strike-slip. Even though the fault is buried over 10 km in depth, the earthquake caused 117 death, 550 injuries and many building collapses. We use dynamic rupture models to reproduce the inversed rupture process to investigate source effects of ground motion and to shed lights on why the rupture on such an unfavored fault plane caused so much damage. In our best fit model, inside low-velocity sedimentary Tainan basin, the uniform velocity structure works well for the rock sites but 3D velocity structure is important to generate the large horizontal ground motions recorded in the Tainan basin during the earthquake. The station in the Tainan area got the most severe damage which could be caused by the combination of rupture directivity and basin effect.

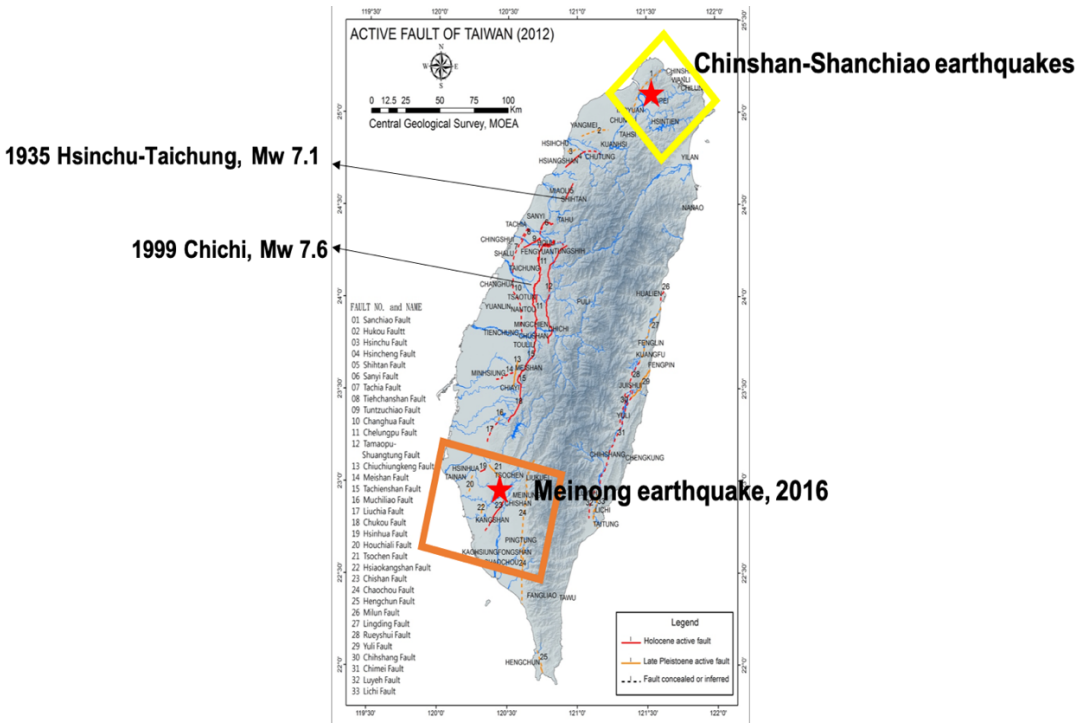

Figure 1.1. Surface traces of active faults in Taiwan in bold or dashed red and yellow lines. Published by the Central Geological Survey in 2012. The yellow and orange squares show the location of the study area in the study. Reprinted from Lin *et al.* [2012].

2. METHODOLOGY

The chapter discusses the finite element method (FEM) used to simulate dynamic rupture processes, seismic wave propagation and correspondent ground motion. In general, two types of models are used to evaluate earthquake source process and ground motion: kinematic source models and dynamic rupture models. A kinematic source model prescribes rupture velocities and slip histories to model an earthquake rupture. In a dynamic rupture model, given initial stress conditions on an earthquake fault and a friction law to control traction evolution, quantities such as slip and rupture velocity are solved and physically constrained. Kinematic models tend to overpredict ground motion levels. Olsen *et al*. [2006] and Olsen *et al*. [2008] use kinematic models and dynamic rupture models to simulate hypothetical earthquakes in southern California, respectively. They show that kinematic models will overpredict ground shakings because of the coherent waves induced by prescribed rupture velocities. In addition, the FEM show advantages to other methods in modeling geometrically complex faults, such as the Chinshan-Shanqiao fault in northwestern Taiwan which has at least one bend along dip direction [Chen *et al*., 2014] and potential bends along strike discussed later. The FEM can also incorporate realistic velocity structures, such as low velocity sedimentary basin, with dynamic rupture models to account for the non-linear coupling of the source and path processes.

For both the Meinong earthquake and scenario earthquakes of the Chinshan-Shanchiao fault system, we use FEM EQdyna [Duan and Oglesby, 2006; Duan and Day, 2008; Duan, 2010, 2012; Liu and Duan, 2018] to model dynamic ruptures. EQdyna is a

well-developed parallel FEM designed for simulating dynamic ruptures, seismic wave propagation and ground motion. It has been validated against the benchmark problems of the SCEC/USGS Spontaneous Rupture Code Verification Project [Harris *et al*., 2018].

2.1. EQdyna: FEM to Simulate Dynamic Ruptures and Ground Motion

EQdyna is a FEM to model spontaneous dynamic rupture on geometrically complex faults and ground motions. The 2D version of EQdyna is first developed in 2006 to investigate multicycle dynamics of geometrically complex faults [Duan and Oglesby, 2006; 2007], off-fault damage induced by rupture dynamics [Duan and Day, 2008]. 3D version of EQdyna is developed to model spontaneous rupture propagation in large earthquakes such as 2008 Wenchuan earthquake [Duan, 2010a] and 2011 Tohoku-Oki [Duan, 2012]. Several new features including Perfectly Matched Layer (PML) absorbing boundary, 3D MPI and Q attenuation model have been implemented to evaluate ground shaking from scenario earthquakes in North China Basin [Duan *et al*., 2017; Liu and Duan, 2018]. In the attenuation model, the memory variables are coarse grained, that is, redistributed in such a way that only a single relaxation time is represented at each node point (and therefore a single memory variable per stress component is required).

EQdyna solves elastic or elastoplastic dynamic problem containing fault surface discontinuity and the free earth surface. The equations of motion for the elastic medium is

$$\rho \ddot{\boldsymbol{u}} = \boldsymbol{\nabla} \cdot \boldsymbol{\sigma} + \rho \mathbf{b} \qquad (2\text{-}1)$$

in which $\boldsymbol{\sigma}$ is the stress tensor, $\boldsymbol{u}$ is the displacement vector, $\mathbf{b}$ is the body force vector, ρ is density, and double dots on $\boldsymbol{u}$ represent the second derivative in time (thus the

acceleration). The first term on the right-hand side of Equation (2-1) with the dot product of the operator ∇ and the stress tensor gives the divergence of the stress field, resulting in a vector.

EQdyna follows the standard FEM procedure [Hughes, 2000] to solve the equations of motion. Duan and Oglesby (2006) gave a brief description of the procedure. After discretizing in space, a matrix equation can be obtained from (2-1)

$$\mathbf{M}\ddot{\boldsymbol{u}} + \mathbf{K}(\mathbf{u} + q\dot{\mathbf{u}}) = \mathbf{F} \qquad (2\text{-}2)$$

where **M** and **K** are the mass matrix and the stiffness matrix, respectively, **F** is the vector of applied forces, q is a stiffness-damping parameter used to damp high-frequency noises. q can be specified through a non-dimensional parameter β [Duan and Day, 2008], so that q =β Δt, or equivalently,

$$\mathrm{q} = \beta\alpha\Delta\mathrm{z}/v_p \qquad (2\text{-}3)$$

where Δz is the minimum element size along z-axis , α is the Courant-Friedrich-Lewy number and v_p is the P wave velocity. We use lumped mass matrix M, which is diagonal, and explicit time integration scheme [Hughes, 2000]. Equation (2-2) can be solved by the central difference time integration method,

$$a_n = \boldsymbol{M}^{-1}(F_n - \boldsymbol{K}(u_n + qv_n)) \qquad (2\text{-}4)$$

$$v_{n+1} = v_n + a_n\Delta t \qquad (2\text{-}5)$$

$$u_{n+1} = u_n + v_{n+1}\Delta t \qquad (2\text{-}6)$$

where the simulation time step Δt should be small enough: $\Delta t = a(\Delta\mathrm{z})/v_p$, 0<a<1, Δz is the minimal element size.

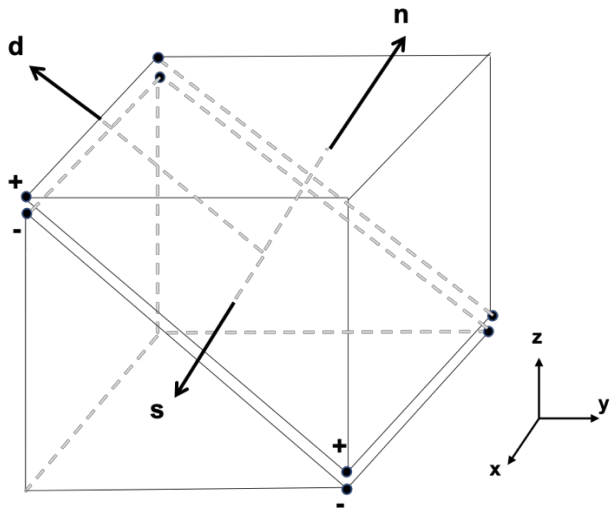

Figure 2.1. Illustration of split nodes on the two sides of the faults plane. To apply the traction-at-split-node (TSN) method in EQdyna, a local coordinate system according to three axes of unit vectors (normal $\vec{n}$, strike $\vec{s}$, dip $\vec{d}$) on the fault plane are used instead of the global coordinate system (x, y, z). The figure shows two fault planes to illustrate the split-node method.

Figure 2.1 shows how we apply the Traction-at-Split-Node (TSN) method. The nodes on the fault surface are split into plus-side nodes and minus-side nodes. The velocity and displacement discontinuities between the two sets of nodes are slip rate and slip, respectively.

2.2. Friction Law, Material Property and Initial Stresses

A spontaneous rupture model needs some essential ingredients, including the fault geometry, friction law, material property (velocity and density structures) and initial stress field.

Laboratory experiments on rock frictional sliding at high-speed slip [Okubo and Dieterich, 1986] and of numerical modeling of dynamic rupture with laboratory-derived constitutive laws [Okubo, 1989] suggest that slip-weakening is the prevailing constitutive behavior during dynamic ruptures [Guatteri and Spudich, 2000]. Therefore, we adopt the slip weakening law [Ida, 1972; Andrews, 1976a, 1976b; Day, 1982] to model dynamic ruptures. In the slip-weakening law, the fault begins to rupture when shear stress reaches to the shear strength. As the slip grows to the critical slip-weakening distance D_0, the shear stress drops linearly from the shear strength to sliding shear stress or equivalently the friction drops from μ_s to μ_d as shown in Figure 2.2. The fault edges (except the free surface) are pinned by a high static frictional coefficient. To initiate the rupture, we prescribe a nucleation patch within which the rupture is forced to propagate at a fixed low speed. Outside the nucleation patch, the rupture propagates spontaneously. In the case of Meinong earthquake, the nucleation patch is chosen as the inversion results of Lee *et al.*(2016). In the case of potential earthquakes of Chinshan-Shanchiao fault, the nucleation patch is chosen in the center of the mid-lower fault segment. The different locations of the nucleation patch should affect the rupture propagation and ground motion of the potential earthquakes, but we only consider this case for now to study and compare results' sensitivity to various physical parameters.

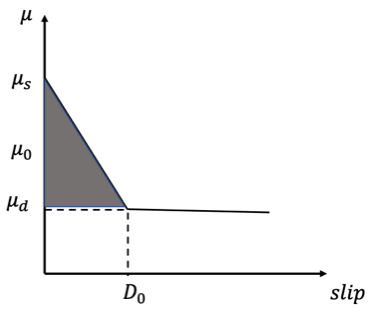

Figure 2.2. Slip weakening law to govern the rupture process. The friction μ drops from the static value μ_s to the sliding value μ_d over a critical distance D_0.

The velocity model we use is the 3D P-wave velocity model of Taiwan from travel-time tomography from Chen *et al*. [2012], named Taiwan.TTT.KWR.2012. This model is based on a travel-time tomographic method from active- and passive-source experiments of Taiwan Integrated Geodynamic Research (TAIGER) and other permanent seismic networks. For initial stress set up, we use the depth-dependent vertical principal stress and horizontal principal stress for scenario earthquakes on the Chinshan-Shanciao fault. Their ratio is a constant of R. We will study the rupture propagation and ground motion simulation based on various R values and different sets of principal stresses, which we will discuss later. The effective vertical principle stress σ_z is,

$$\sigma_z = \int (\rho - \rho_w) g dz$$

where ρ and ρ_w are the densities of rock and fluid, respectively, and g is the gravity acceleration. Then we resolve the stress tensors to normal and shear stresses on the fault according to fault local strikes and dips.

A stress ratio R is defined by a nominal frictional coefficient μ_0 that characterizes the initial stress state on the fault plane [Duan, 2010]

$$R = \sigma_{max}/\sigma_{min} = [\sqrt{(1+\mu_0^2)} - \mu_0]^{-2}$$

where σ_{max} and σ_{min} are the maximum and minimum principal stresses, respectively. In the study of the Chinshan-Shanchiao fault, it's a normal fault system. The largest compressive stress σ_1 is the vertical stress, while σ_2 and σ_3 are the horizontal stresses. Here we set $\sigma_2 = \sigma_3$. We also try to setup initial stresses by focusing on the stress drops of various patches to reproduce the 2016 Meinong rupture process.

2.3. Perfectly Matched Layer (PML) Absorbing Boundary

The technique of perfectly matched layer is developed to absorb outgoing electromagnetic wave travelling towards model boundaries [Berenger, 1994]. The method is efficient on a discretized model. Collino and Tsogka [2001] incorporate the technique for elastodynamic wave propagation in a stress-velocity formulation. Their formulation provides a groundwork for both 3D staggered-grid velocity-stress finite-difference methods [Festa and Nielsen, 2003] and explicit FEM [Ma and Liu, 2006]. Liu and Duan [2018] adopts the formulation of Ma and Liu [2006] to incorporate PML in EQdyna.

2.4. Parallel Computing

With rapid development of modern high-performance computing (HPC) systems, particularly clusters with CMPs (Chip Multi-Processors), parallel computing is a powerful tool for dynamic rupture and ground motion simulations at large scales. Parallel computing allows exploration of rupture complexities observed in large earthquakes and enables high-frequency deterministic ground motion simulations. 3D version of EQdyna is parallelized using Message Passing Interface (MPI) in three dimensions, which significantly increases the scalability of EQdyna on HPC. It allows us to perform high-resolution 3D simulation to capture rupture details and fine velocity structures.

The Texas A&M High Performance Research Computing (HPRC) group provides technical expertise and high-performance hardware to expedite large-scale scientific computation. There are three major clusters for high performance computation, Ada, Terra and Curie. In the study, we mainly use the Ada cluster to run simulations. Ada is an Intel x86-64 Linux cluster with 852 compute nodes (17,340 total cores) and 8 login nodes. In the Chinshan-Shanchiao fault project, the element size is 200m by 200m by 61m along the x, y, z directions, respectively. There is a total of 235.8 million elements in each model. 400 cores with 20 nodes with 1500 Mb per node memory are used for each simulation.

3. DYNAMIC RUPTURES OF THE 2016 M_L 6.6 MEINONG EARTHQUAKE

3.1. Introduction

On the morning of February 6th, 2016, at 3:57:26.08 local time (UTC+8), the M_L 6.6 Meinong earthquake occurred in southern Taiwan. According to the Central Weather Bureau (CWB) of Taiwan, the hypocenter was at 14.6 km depth and the epicenter (22.92° N, 120.54° E) was in the district of Meinong town. Many buildings in the Tainan area suffered serious damage including several collapses. The Meinong earthquake caused 117 deaths and more than 500 injuries. Nearly all the deaths were caused by the collapse of a 16-floor reinforced concrete building in Tainan city [Lee *et al*., 2016]. The location of the fault relative to Taiwan island and stations that record seismograms are shown in Figure 3.1. Tainan city where serious damage occurred is also shown in Figure 3.1.

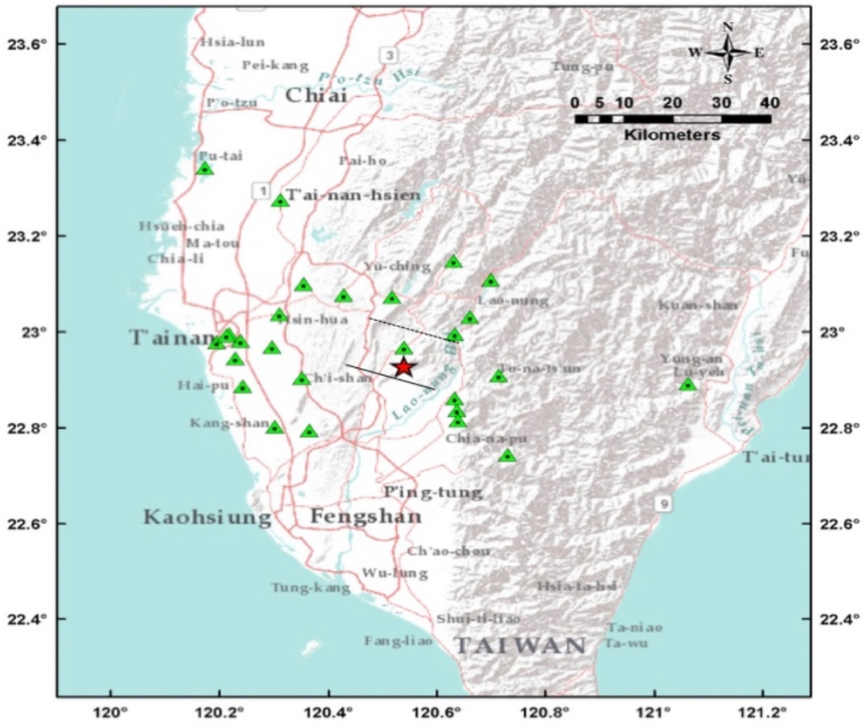

Figure 3.1. Research region and southern Taiwan. Epicenter of the Meinong earthquake is indicated by the red star as (22.92° N, 120.54°). The top (buried) and bottom traces of the fault are shown by the solid and dashed lines. The fault is 50-km along strike and 40-km along dip. The strike of the fault is 281°. The dip angle of the fault is 24°. The stations with recorded seismograms are indicated by green triangles. Important cities in the region are shown. The Tainan city suffered the most damage even though that it is tens of kilometers away from the fault and the earthquake is moderate in size.

The earthquake occurred on a buried and low angle dipping fault with dominant left-lateral strike slip [Lee *et al*., 2016]. The fault is buried below 8 km depth and has a 24˚ dipping angle [Lee *et al*., 2016]. However, the dominant slip is left-lateral rather than thrusting slip with a maximum 1.2 m. How does a moderate earthquake of left-lateral slip on such a low dipping and deeply buried fault cause severe damage in the Tainan city tens kilometers away? Several factors have been proposed that includes directivity effect, local

site effects, and/or a triggered subevent. Diao *et al.* [2018] adopt source fault modeling and the joint source inversion for the earthquake and indicate that the rupture propagated from the hypocenter toward the WNW in the main rupture area, showing a strong rupture directivity effect, which generated the large long-period ground motions in the Tainan area. Lee *et al*. [2016] perform a joint source inversion using three data sets (teleseismic data from IRIS-DMC, Real-time Seismic Network data from CWB, and local broadband data from BATS), which shows two asperities and strong rupture directivity toward N79W. The rupture area is about 25 by 25 kms along dip and strike. The rupture lasts about 14 seconds. Inversed slip distribution and rupture process from Lee *et al*. [2016] are shown in Figure 3.2a and 3.2b. Asperity I is the largest with a size of 8 by 15 km along dip and strike that is dominated by left-lateral slip. The maximum slip is 120.2 cm. Asperity II appears to be a relatively isolated slip patch that is in the shallower portion of the ruptured fault plane west to the hypocenter. The size of the asperity is about 6 by 10 km along dip and strike, respectively, and the maximum slip is about 50 cm. Jian *et al*. [2017] adopt the back-projection method and show that there are two asperities on the fault plane and a strong rupture directivity effect toward northwest. The rupture length (~17 km) and the duration (~7 s) are both shorter than those in Lee *et al.* [2016]. The rupture directivity points more northwestwards than that in Lee *et al*. [2016].

.

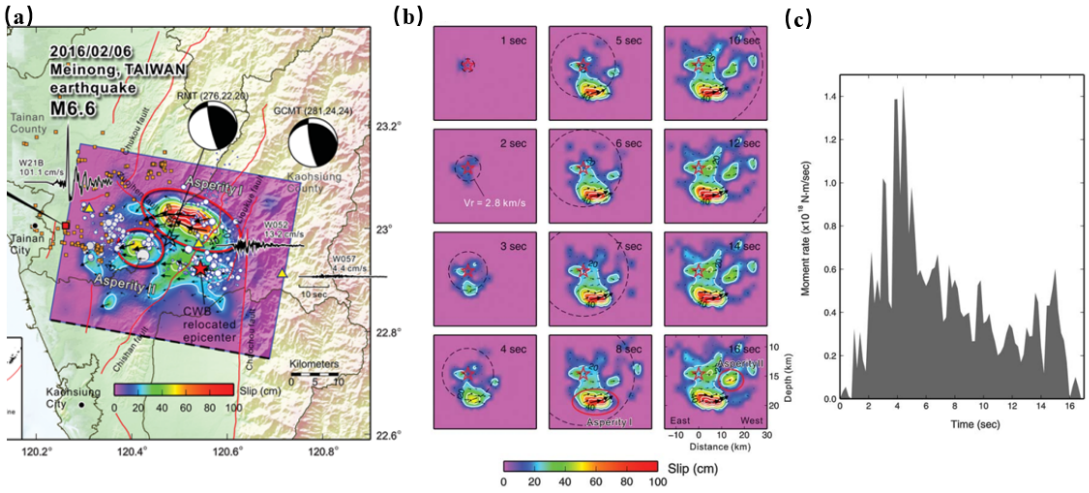

Figure 3.2. (a) Inversed slip distribution of the Meinong earthquake. (b) Inversed slip evolution and rupture process. (c) Inversed moment rate history [Lee *et al*., 2016].

Kinematic source models for the earthquake provide us with images of how earthquake rupture propagates co-seismically, by fitting various datasets. However, dynamic ruptures could present a rupture process with slip and stress physically constrained by friction law. In this study, we try to first reproduce the inversed rupture process with dynamic rupture models governed by the slip-weakening law. We compare simulated seismograms to recorded ones. We use a uniform velocity structure for dynamic ruptures. Finally, we analyze results and provide possible explanations to the anonymously large amplitude of ground shaking in Tainan city.

3.2. Methods and Models

We use EQdyna to model dynamic ruptures and wave propagation. A dynamic rupture model has several ingredients: the fault geometry, material properties, initial stress field, and the friction law. We'll elaborate them in detail.

3.2.1. Model size and fault geometry

We build a 3D Cartesian coordinate system using the epicenter 22.92° N, 120.54° E of the Meinong earthquake as the origin and the fault-strike direction as the x-axis. The fault-normal direction is y-axis and the vertical direction z-axis. According to Lee *et al*. [2016], the fault is 50 km along strike and 40 km along dip and the top of the fault is buried at 8 km depth. The fault strikes towards 281° and has a dipping angle of 24°. In this coordinate system, the fault extends from -25 to 25 km along x-axis, from 0 to 24 km along y-axis, from -8 to -28 km along z-axis. The hypocenter (x_0, y_0, z_0) is (6.0 km, 8.79 km, -14.6 km). Except the free surface, model boundaries should be extended tens of kilometers away from the fault because the fixed boundaries may affect solutions on the fault if they were too close to the fault. The model ranges from -50 to 50 km along x, from -40 to 60 km along y-axis, from -60 to 0 km along z. The coordinate system and the fault geometry are shown in Figure 3.3. Hexahedron elements, whose ordering of nodes is shown in Figure 3.4b, are used and the edges are 0.2 km, 0.2 km and 0.089 km in x, y, and z, respectively. If the hexahedron were bisected by the fault, the hexahedron is degenerated into two wedge elements. Technically, we merge nodes 7 and 6, nodes 5 and 8 to get the wedge element from a hexahedron as shown in Figure 3.4b [Hughes, 2000]. Figure 3.5 is

a schematic diagram to show the meshes around the dipping fault and in the volume surrounding the fault.

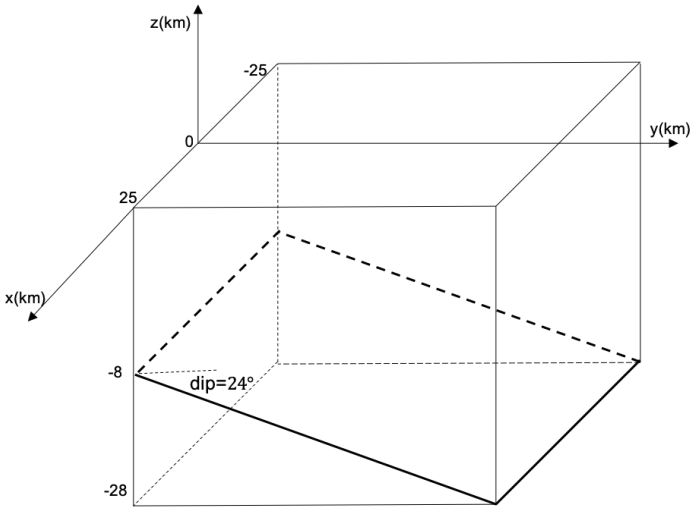

Figure 3.3. The coordinate system and the fault geometry in the model. The bold solid and dashed lines compose the fault plane. The fault ranges from -25 to 25 km along x and from -8 to -28 km in z direction. The dipping angle is 24˚. The positive x direction is S79E.

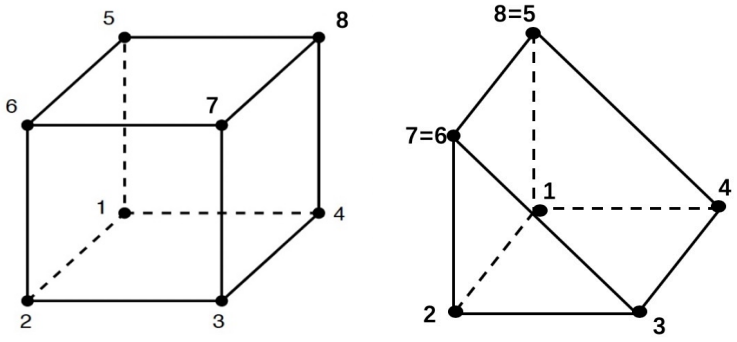

(a) Brick Element (b) Wedge Element

Figure 3.4. (a) The ordering of nodes in a hexahedron element; (b) The ordering of nodes in a degenerated wedge element to model the dipping fault geometry.

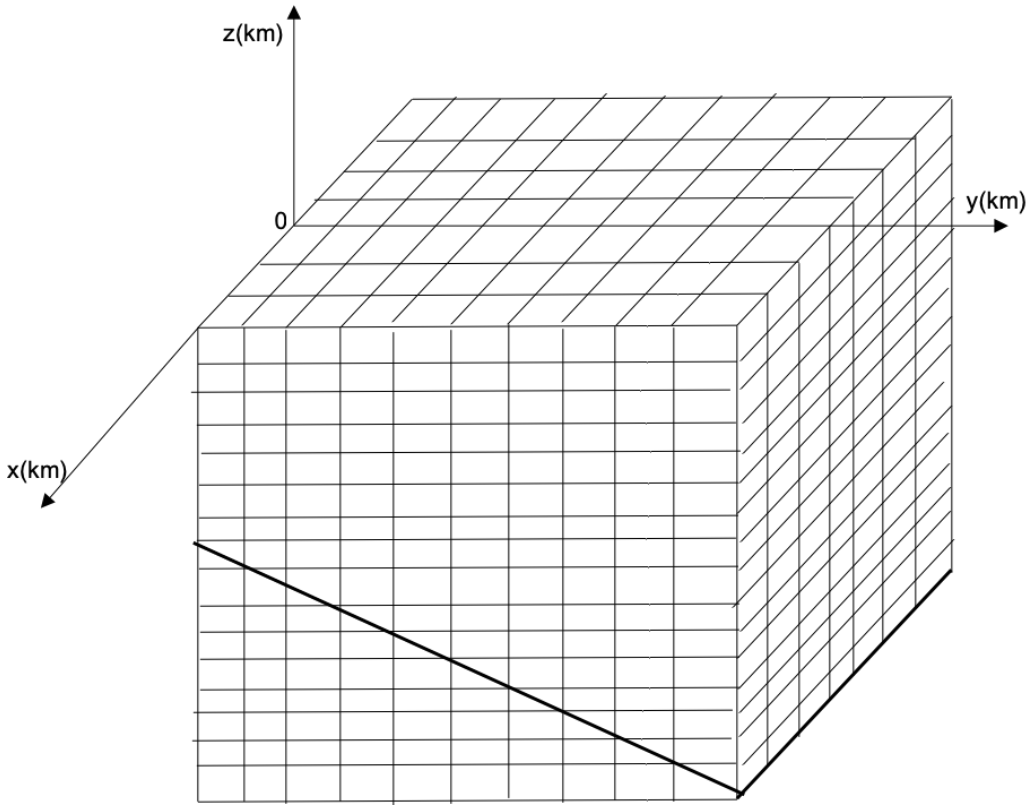

Figure 3.5. A schematic mesh plot showing the degeneration of hexahedrons into wedges to model the shallow dipping geometry. dx is the spatial interval along x-axis, dy along y-axis, and dz along z-axis.

3.2.2. Material properties

We first apply uniform material properties to model dynamic ruptures. The P wave and S wave velocities are 6000 m/s and 3464 m/s, respectively. The density is 2670 kg/m^3. We then visualize a realistic 3D P-wave velocity model [Huang 2014] and put stations together with the detailed velocity structure. Huang [2014] use a joint inversion joint of datasets from several permanent networks and temporal arrays. A total of 1210 stations are used to yield the 3D V_p , V_s and V_p/V_s structures. The spatial interval along latitude and longitude are both $0.08°$. Spatial intervals along the vertical direction vary and the data

are at 0, 0.5, 3, 6, 10 km depths and later at an interval of every 5 km. We name the velocity structure Huang2014. Figure 3.6 (a) and (b) shows P-wave and S-wave velocity structures at various depths from Huang2014, respectively. To calculate the density, we adopt the polynomial regression fittings proposed by Brocher [2005] which presents empirical relations among V_p and ρ, that can be used to infer for the entire Earth's crust. The fitting equations are based on the handpicked ρ and V_p values from the compilations of sources of California samples, like wireline borehole logs for a variety of rocks, vertical seismic profiles (VSPs), laboratory or field measurements on hand samples, and *in situ* estimates from seismic tomography studies [Brocher, 2005]. Equation (3-1) is the empirical relationship for density ρ as a function of V_p. V_p is in km/s. It is valid for V_p between 1.5 and 8.5 km/s.

$$\rho(g/cm^3) = 1.6612V_p - 0.4721V_p^2 + 0.0671V_p^3 - 0.0043V_p^4 + .000106V_p^5 \quad (3\text{-}1)$$

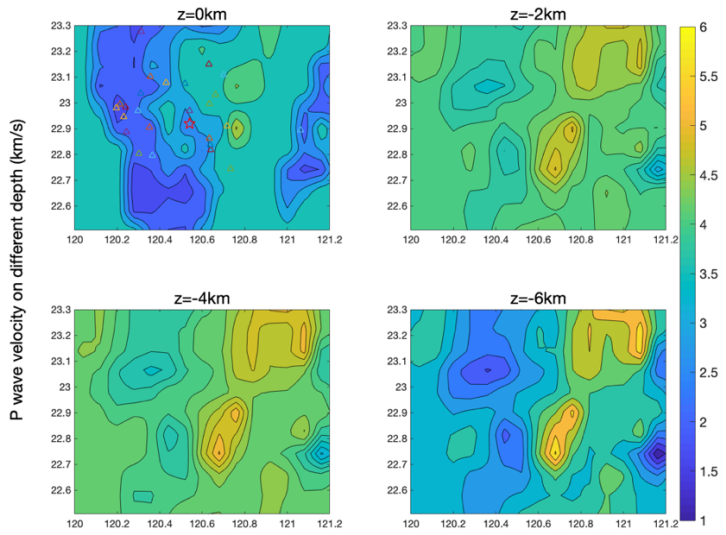

(a) P wave velocity at different depths

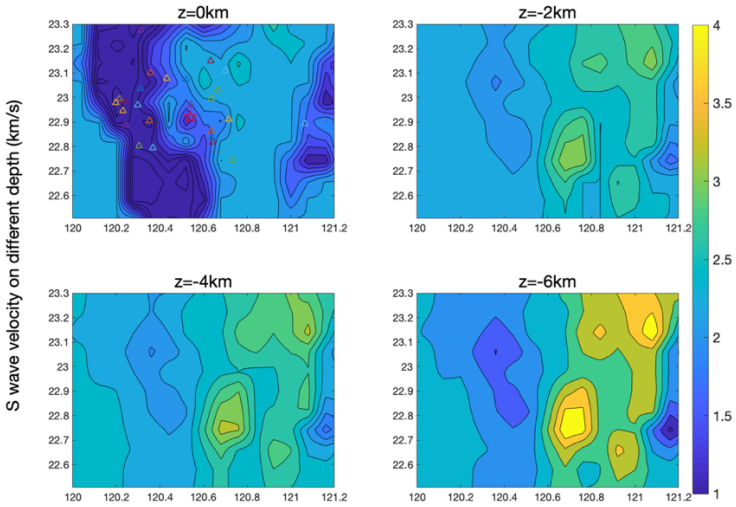

(b) S wave velocity at different depths

Figure 3.6. (a)P wave velocity model at depths of 0, 2, 4, 6 km from Huang *et al.* [2014]. The color bar shows P wave velocity in km/s that ranges from 1.68 to 5.5 km/s. (b) S wave velocity model at depths of 0, 2, 4, 6 km from Huang *et al.* [2014]. The color bar shows S wave velocity in km/s that ranges from 0.47 to 3.3 km/s. We truncate it to 0.5km/s. The vertical axis is latitude and the horizontal axis longitude. Stations that recorded seismograms are triangulars. The epicenter is the red star.

3.2.3. Initial stress setup

Initial stresses on the fault before earthquakes are critical while are not well constrained. Because of the low dipping angle of the fault and its unusual dominant left-lateral slip, we focus on adjusting stress drops in various patches to fit the inversed slip distribution and rupture process rather than judging the absolute values of frictional coefficient. Therefore, we set the initial normal and shear stresses on the fault -50 MPa and 30 MPa, respectively. Negative normal stress indicates compression. Stress drops vary with locations. Based on the slip distribution inversed from Lee *et al*. [2016], we assign two patches with relatively large stress drop representing the two asperities as shown in Figure 3.2a. The stress drop distribution before the rupture of our best model is shown in Figure 3.7. The distribution is obtained by trial-and-error to fit to the correspondent slip distribution, moment rate history, and rupture time contour of the inversed results. The method of trial-and-error we use here is mainly changing the parameters little by little to fit the inversion results. For example, to control the rupture velocity, we adjust the value of D_0 within the range of 0.2 to 1. For a fixed initial friction coefficient μ_0, we change the sliding friction coefficient μ_d to get close to the inversed stress drop.

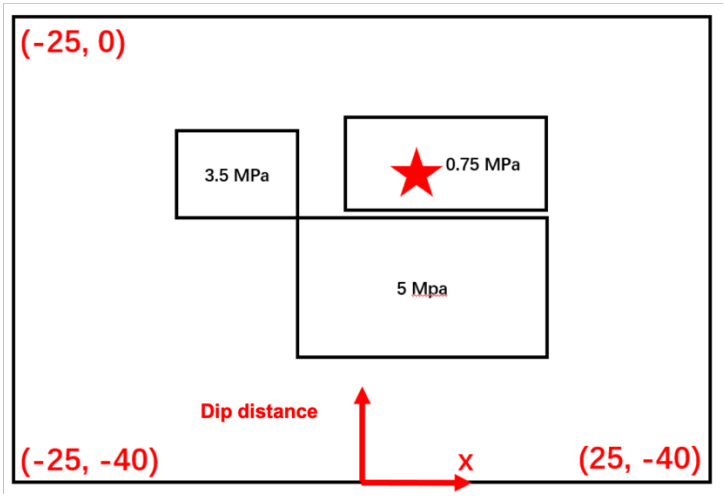

Figure 3.7. The stress drop distribution on the fault plane in the best model. Two asperity patches have stress drops of 5 and 3.5 MPa, respectively. The nucleation zone has a stress drop of 0.75 MPa. The top of the fault is buried at 8 km depth. The red star is the hypocenter.

3.2.4. Friction law and choice of parameters

Governed by the slip-weakening law, the fault begins to rupture when shear stress reaches to the shear strength. As the slip grows to the critical slip-weakening distance D_0, the frictional coefficient drops from the static value μ_s to the dynamic value μ_d. One issue is how to choose D_0, which is not well constrained by observations. In ground motion simulations, D_0 is generally taken as a constant over the whole fault plane and it ranges from 0.2 m to 1 m [Olsen, 1997; Oglesby and Day, 2002; Olsen *et al*., 2008; Olsen *et al*., 2009].

Guatteri and Spudich [2000] show that under the context of the slip-weakening law, if a stress drop distribution is given, it is the apparent fracture energy distribution (shaded area in Figure 2.2) that controls the rupture velocity and the low frequency ground motions (<1.6 Hz) because of the strong trade-off between the D_0 and the stress excess

(shear strength minus initial shear stress). They simulate two dynamic ruptures of similar apparent fracture energy but different D_0 and strength excess. We choose $D_0 = 0.4\ m$ for our models. We try to fit the inversed rupture time contour.

To initiate the spontaneous rupture, we artificially allow the rupture to propagate at a fixed slow speed within the nucleation zone. Outside the nucleation patch, the rupture propagates spontaneously with rupture speed part of the solution. To ensure numerical stability for the models, we calculate the time step as in the formula:

$$\Delta t = \alpha * dz/\max(Vp) \qquad (3\text{-}2)$$

where *dz* is the element size along vertical direction and max(Vp) is the maximum P wave velocity in the model. In the uniform velocity model, Vp is 6000 m/s. α is the coefficient chosen as 0.5. Therefore, we choose *dt* as 0.005 s. We run the code to t = 50 s to take account of wave propagation towards the farthest station with seismograms. Table 3.1 show the friction coefficients of the model.

Table 3.1 Friction coefficients for the model

	μ_s	μ_0	μ_d
Asperity 1	**0.62**	**0.6**	**0.5**
Asperity 2	**0.62**	**0.6**	**0.53**
Background	**0.62**	**0.6**	**0.6**
Hypocenter	**0.62**	**0.6**	**0.585**

3.3. Results and Analysis

Figure 3.8 show the rupture time contour (a) and final slip distribution (b) from our best model. The rupture time, which is defined when the slip rate at the on-fault location reaches 0.001 m/s, and final slip distribution roughly match the inversions (Figure 3.2a and 3.2b). As shown in Figure 3.8a, after the rupture propagates from the hypocenter, it quickly breaks Asperity I before t = 6 s and then it ruptures Asperity II between t = 6 s and t = 10 s. We also reproduce the two asperities in Figure 3.8b with the maximum slip in Asperity I about 1.4 m, slightly larger than the inversed 1.2 m maximum slip. The total moment magnitude is 6.63 from our model, which is slightly larger than the M_w 6.52 from the inversion as in Figure 3.2 (b).

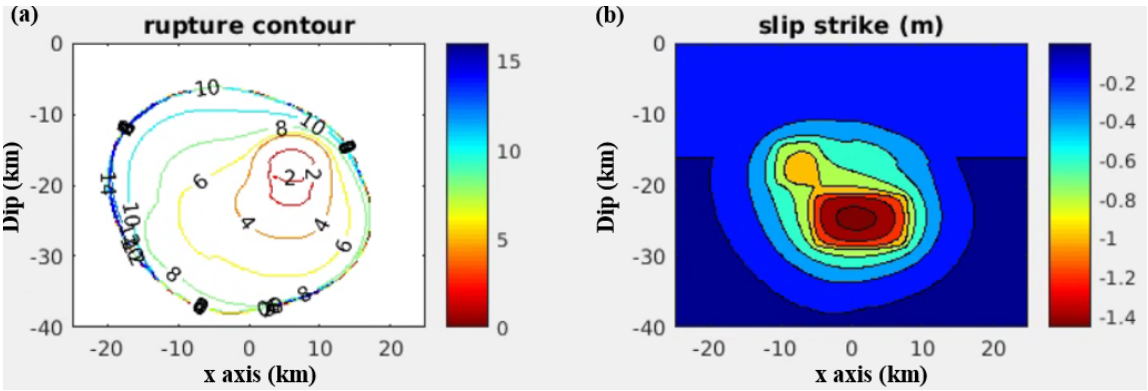

Figure 3.8. (a) Rupture time contour and (b) final slip distribution of the best model.

Figure 3.9 shows the moment rate history of the best model. It shows a peak of moment rate around 5 ~ 6 s after the rupture and a second peak around t = 8 s. It captures the dominant energy release of the Meinong earthquake according to Figure 3.2c. We

haven't reproduced the later peak at about t = 15 s. However, we note that it is the first two waves of energy release contribute most to the ground motion.

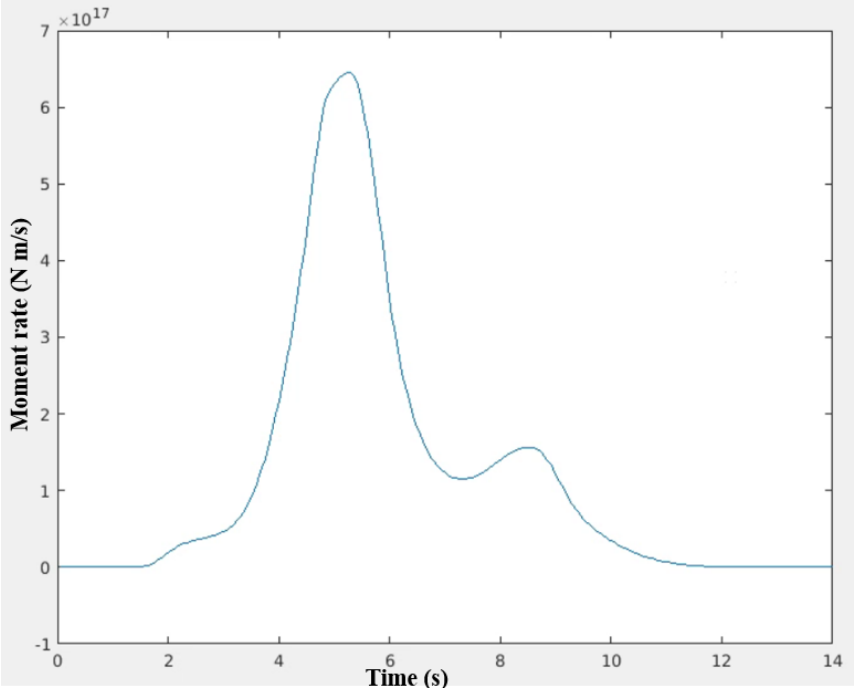

Figure 3.9. Moment rate history of the best model.

Figure 3.10 shows the Vp velocity structure at the free surface and numbered stations where seismograms have been recorded. We will show comparisons between our simulated seismograms and the records which are low-pass filtered below 0.5 Hz at some stations. The station numbers and their correspondent names are also shown in Figure 3.10. There are two groups of stations. One group includes Stations No. 13-15 and 17-20, which are on rocks with relatively high Vp (i.e., rock sites). The other group includes Stations No. 1 and 3, which are located inside low-velocity sedimentary basins.

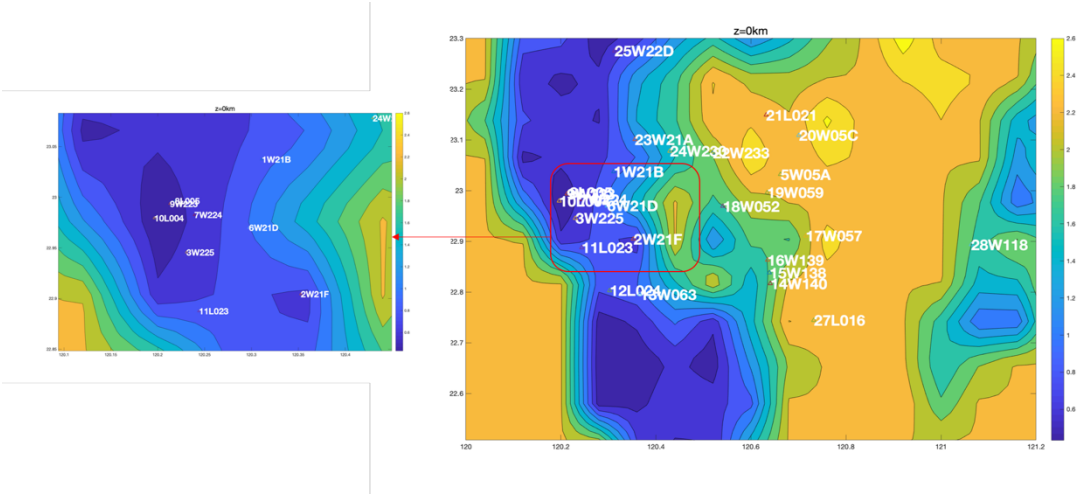

Figure 3.10. Vp velocity structure at the free surface with numbered stations. There are two groups of stations from Taiwan P-alert strong motion network (Wu et al., 2013). One group includes Stations No. 13-15 and 17-20, which are on rocks with relatively high Vp (i.e., rock sites). The other group includes Stations No. 1 and 3, which are located inside low-velocity basin. The left small figure is enlarged area in the red rectangular area in the right large figure.

Firstly, uniform velocity structure is applied in the model. The results are shown from Figure 3.11 to Figure 3.15. Figure 3.11, 3.12, 3.13 and 3.14 show comparisons between simulated and recorded seismograms in 0~0.5 Hz in three directions at Station W063 and W140, W138 and W057, W052 and W059, and W05C and L02, respectively. Based on Figure 3.10, these stations are on rock sites except that Station W063 lies on the edge of the basin. The PGVs in all three directions on rock sites are at similar magnitudes (several cm/s). Our simulated seismograms capture the waveform shapes and PGVs of recorded seismograms on these rock sites. It means the uniform velocity structure dynamic rupture model works well for the rock sites.

At Station W063 (Figure 3.11a), our simulated seismograms match the PGVs of recorded seismograms. But we note that the recorded waveforms show some dominant

long-period basin-induced surfaces waves that our uniform velocity structure cannot reproduce.

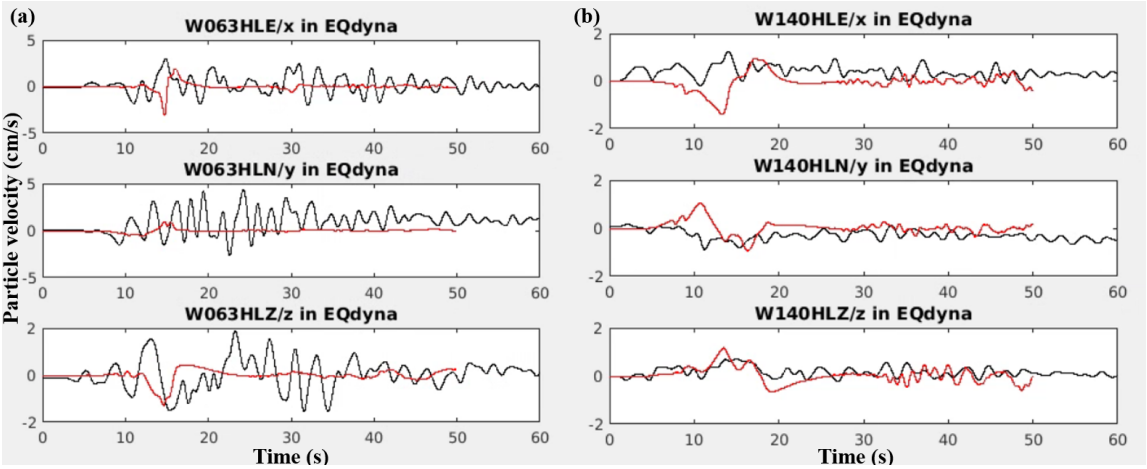

Figure 3.11. Comparisons between simulated and recorded seismograms in 0~0.5 Hz in three directions at Station W063 (a) and W140 (b), respectively. Red and black lines are simulated and recorded seismograms, respectively.

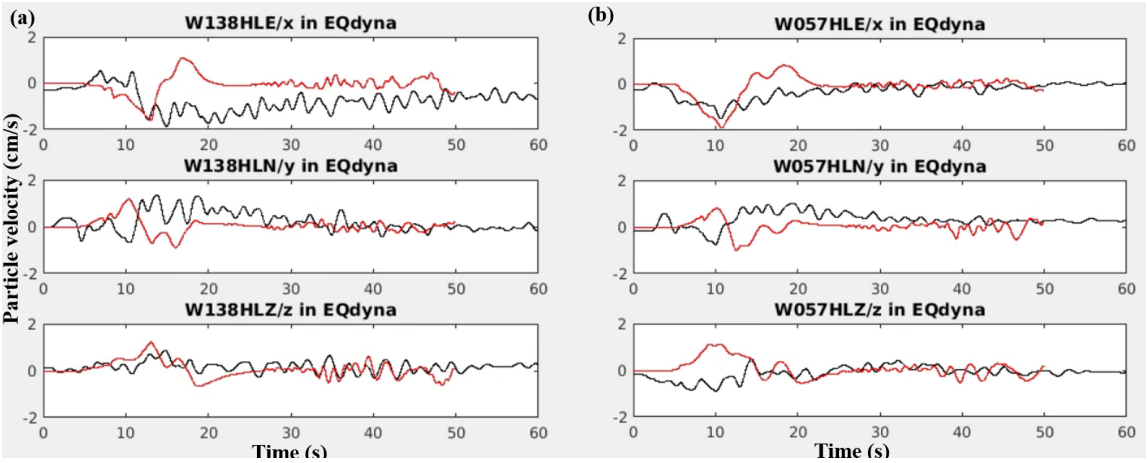

Figure 3.12. Comparisons between simulated and recorded seismograms in 0~0.5 Hz in three directions at Station W138 (a) and W057 (b), respectively. Red and black lines are simulated and recorded seismograms, respectively.

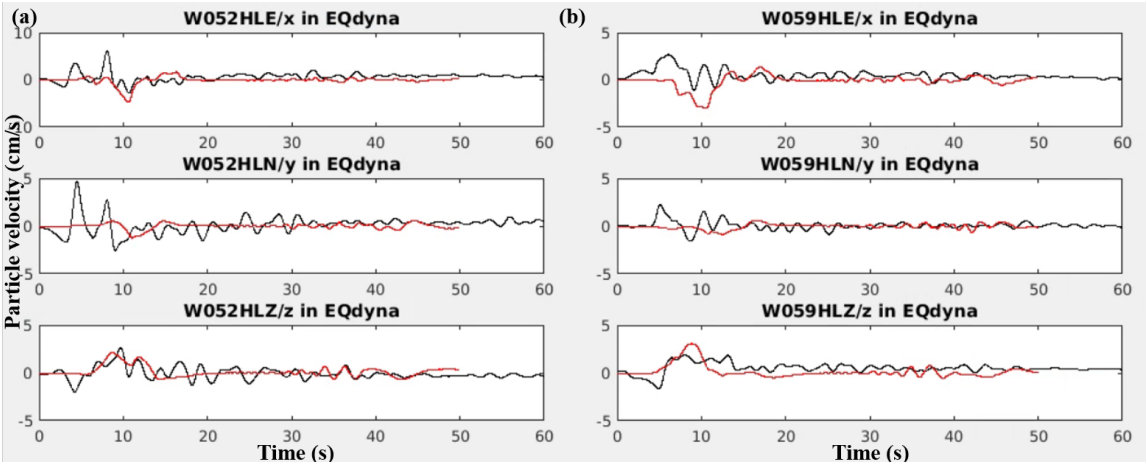

Figure 3.13. Comparisons between simulated and recorded seismograms in 0~0.5 Hz in three directions at Station W052 (a) and W059 (b), respectively. Red and black lines are simulated and recorded seismograms, respectively.

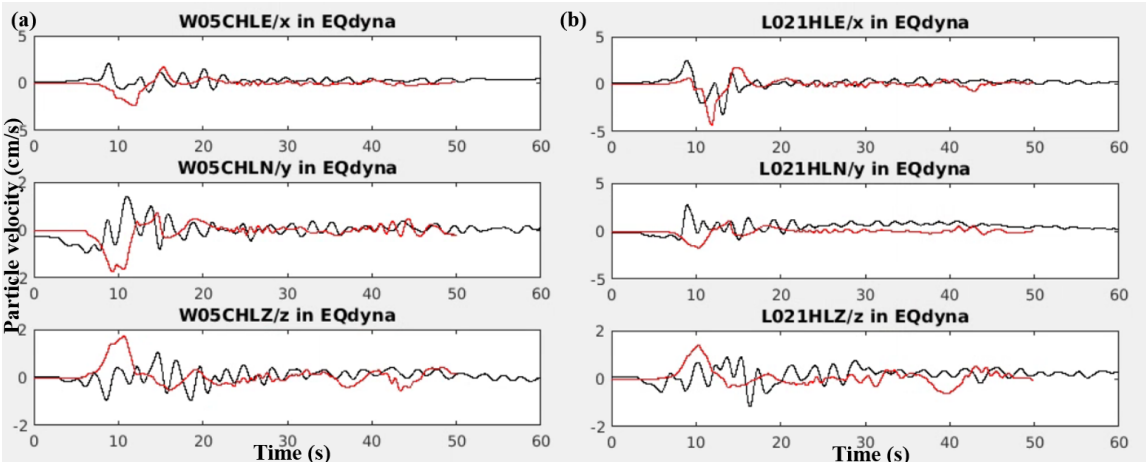

Figure 3.14. Comparisons between simulated and recorded seismograms in 0~0.5 Hz in three directions at Station W05C (a) and L021 (b), respectively. Red and black lines are simulated and recorded seismograms, respectively.

On the other hand, Figure 3.15 show comparisons between simulated and recorded seismograms in 0~0.5 Hz in three directions at Station W21B and W225, respectively. As shown in Figure 3.10, the two stations are located inside the low-velocity basin. We note that the recorded seismograms show extreme large PGVs along horizontal directions but

the PGV in the vertical component remains similar to those on rock sites. Our model with uniform velocity structure can match the PGV in vertical direction but cannot match the horizontal PGVs. It indicates in the recorded seismograms the low-velocity structure play critical roles in causing the extremely large horizontal PGVs inside the Tainan basin.

Figure 3.16 shows the results of two stations, W21B and W225, in the Tainan basin with realistic velocity model. Compared to Figure 3.15 with results of uniform velocity model, the PGVs are larger and matches closer to the recorded seismograms. However, for Station W21B, the horizontal PGVs are much less than the recorded data, which means the extreme large PGVs may be caused by the stronger site effect. Figure 3.17 shows the comparison between simulated seismograms in uniform, realistic velocity model, and recorded seismograms at Stations W21F, W224, L024, L004 and L023 that are all in the Tainan basin. The results are similar to aforementioned stations, W21B and W225, in the basin.

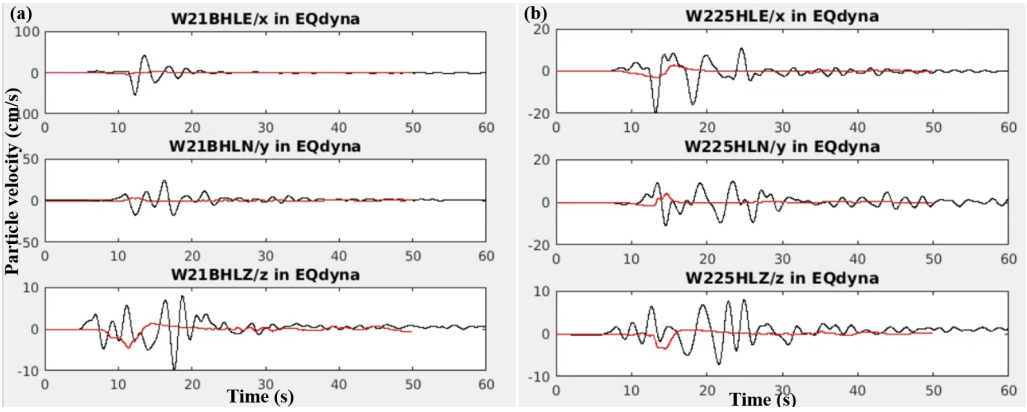

Figure 3.15. Comparisons between simulated and recorded seismograms in 0~0.5 Hz in three directions at Station W21B (No.1) (a) and W225 (No. 3) (b), respectively. Red and black lines are simulated and recorded seismograms, respectively.

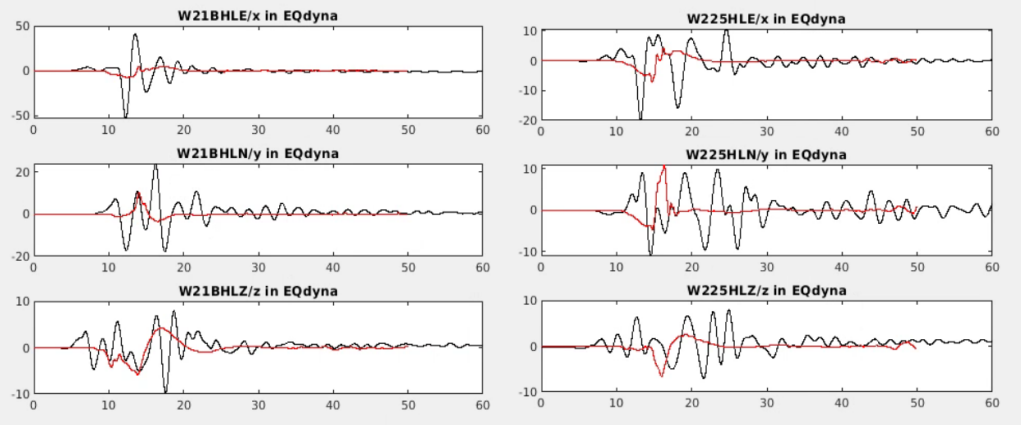

Figure 3.16. With 3D realistic velocity structure, comparisons between simulated and recorded seismograms in 0~0.5 Hz in three directions at Station W21B (No.1) (a) and W225 (No. 3) (b), respectively. Red and black lines are simulated and recorded seismograms, respectively.

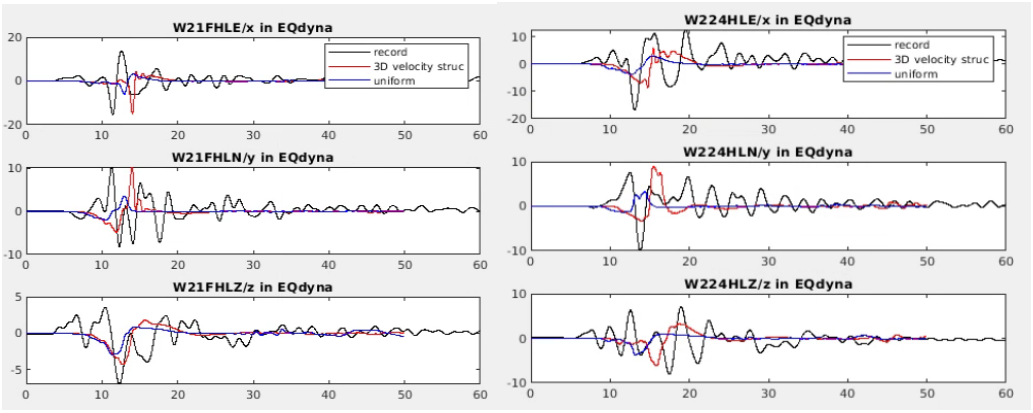

Figure 3.17. Comparisons between simulated seismograms in uniform and realistic velocity mode, and recorded seismograms in 0~0.5 Hz in three directions at Stations W21F , W224, L024, L004 and L023 in the basin. Black lines are recorded seismograms. Blue lines and red lines are simulated seismograms in uniform and realistic velocity model, respectively.

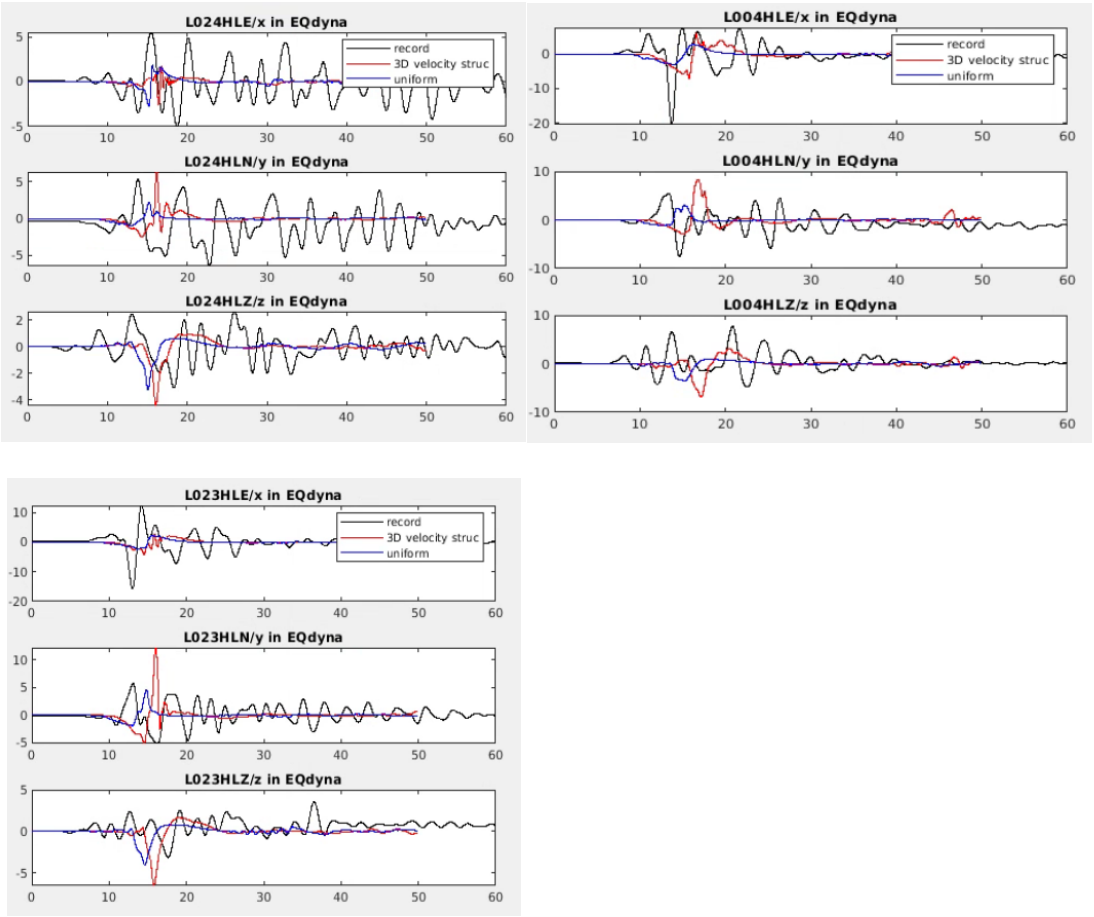

Figure 3.17. Continued.

3.4. Broader Implication

The anonymous ground shaking in the Tainan area far from the source of the earthquake caused a building collapsed and over hundred deaths and injuries. Our dynamic rupture model of the earthquake shows that the combination of basin effect, rupture directivity, characteristics of the deposit layers, etc. can cause severe ground motions some distance away from earthquake faults. This can happen in other places around the world with similar conditions. The study provides some insights for seismic hazard analysis of seismically active regions with sedimentary basins worldwide.

3.5. Conclusion and Discussion

In this study, we use dynamic ruptures to reproduce slip distribution, rupture process and moment rate history from Meinong earthquake kinematic inversions to understand the mechanics that causes the complex rupture details. The earthquake occurs on a buried and shallow dipping fault with dominant left-lateral strike slip with limited amount of thrusting. By trial-and-error, we find in our best fit model two asperities with sizes of 15 by 8 km and of 10 by 6 km that dominate the moment release. The average stress drops in the two asperities are 5.0 and 3.5 MPa, respectively. The whole rupture region is 25 by 25 km. Except for asperities, the region near the hypocenter has a very low 0.75 MPa stress drop. The magnitude of the best model is M_w 6.63 and the maximum slip is 1.4 m, close to M_w 6.52 and 1.2 m from inversions. We apply a uniform velocity structure to simulate ground motions and find the simulated peak ground velocities match the seismograms on rock sites in 0-0.5 Hz. Inside low-velocity sedimentary basin, simulated peak ground velocities also match the recorded vertical peak ground velocities. However, the horizontal peak ground velocities are less than those from records. Therefore, we conclude that the uniform velocity structure works well for the rock sites but 3D velocity structure is necessary and critical to generate large horizontal ground motions during this earthquake in the Tainan basin.

The physics-based source will interact nonlinearly with the complex velocity and density structures, especially when low velocity sedimentary basin is present. Figure 3.10 shows that many stations are located in and at the edge of low velocity sedimentary basins.

Based on previous scenario earthquake simulations with 3D low velocity sedimentary basin structures [e.g., Olsen *et al*., 2008; Day *et al*., 2008; Liu and Duan, 2018], the anonymously large ground shaking that caused severe damage in Tainan could be due to basin-induced surface waves combined with the rupture directivity.

4. POTENTIAL GROUND MOTION FROM SCENARIO EARTHQUAKES ON THE CHINSHAN-SHANQIAO FAULT, TAIWAN, WITH 3D VELOCITY

4.1. Introduction

Seismological studies in Taiwan have traditionally focused on reverse and strike-slip faults because most of the island is located along a convergent boundary that absorbs nearly 85% of the total relative convergence of 82 mm/yr between the Eurasian and Philippine Sea plates [Bos and Spakman, 2003; Yu *et al*., 1997]. Recent geodetic studies indicate that the Taipei area is undergoing northwest–southeast extension at about 0.3–2.1 mm/yr [Yu *et al*., 1999a]. The Chinshan-Shanchiao fault as a normal fault is definitely a special case in the Taiwan area which is mostly under compressional stress condition. The Chinese continental margin and the Luzon volcanic arc collided into each other and caused the mountain building process of the whole Taiwan island [Chai 1972]. However, even if the collision is still pushing up most of the orogen, the north part where the Chinshan-Shanchiao fault is located has been under extension situation [Teng 1996]. Teng [2000] proposes that the extensional stress field in north Taiwan could be caused by that the subduction polarity has flipped from northwest facing in southern Taiwan to southeast facing in northeast Taiwan. As a densely populated region, the potential earthquakes on the Chinshan-Shanchiao fault poise severe seismic hazard to the nearby Taipei basin [McCalpin and Nishenko, 1996; Schwartz and Coppersmith, 1984]. There was once a magnitude 5.5 earthquake occurred in April 1694 and it likely produced a large subsidence in the northwest part of the Taipei basin [Wang *et al*., 1994; Chan *et al*., 2007]. However,

not much information, such as faults slip, is known. Also, another destructive earthquake happened in the Taipei basin in April, 1909. This earthquake caused 9 deaths, 51 people injured, 122 buildings collapsed and 1050 buildings damaged [Wang et al., 2010]. Although it is uncertain when the next earthquake will occur, Wang [2008], Lai [2010] and Huang *et al*. [2007] suggest the fault still has the ability to induce coseismic subsidence in the Taipei basin under present extensional regime of northern Taiwan. According to the estimation of the elastic dislocation models, the potential earthquakes on the Chinshan-Shanchiao fault system could be of a magnitude around 7. Therefore, it is necessary to understand the ground shaking levels from potential earthquakes on the Chinshan-Shanchiao fault.

The geometry of the Chinshan-Shanchiao fault system is shown in Figure 4.1. It is geometrically complex. Several studies have provided guidance on the fault geometry. For example, Chang *et al* [1998] and Lin *et al* [2008]'s fault models are broadly adopted in the various studies [Cai *et al*., 2014; Chen *et al*., 2010; Chen *et al*., 2014]. Wu *et al*. [2012] adopted a more accurate model with two kinks along strike. However, no accurate geometry along dip direction has been proposed until Chen *et al*. [2014]. Chen *et al*. [2014] suggest that the fault plane should be a listric plane which changes the dipping angle from around 75° to 15° in the depth of 3 km. Also, there could be another potential bending in the depth of 8 km, but this bending is not confidently verified yet. Therefore, we use the fault geometry with three fault segments along strike with two fault segments along dip in each of them.

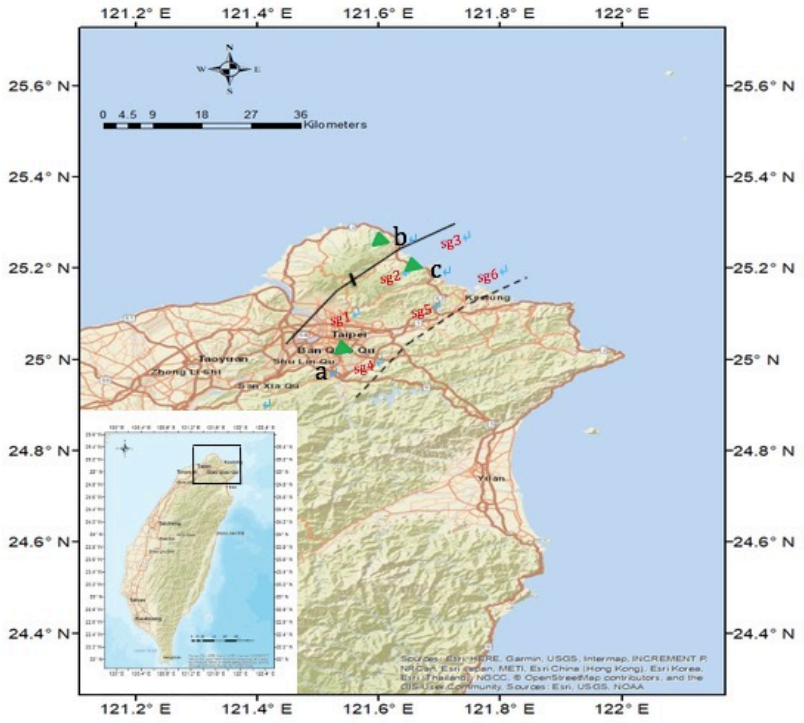

Figure 4.1. Location and geometry of the Chinshan-Shanchiao fault system. The black solid and dashed curves are the top and bottom of the fault, respectively. There are six segments on the fault plane (sg1-sg6). Green triangulars are the three most important sites: a. Taipei 101 tower; b. Jinshan nuclear power plant; c. Kuosheng nuclear power plant. (Adapted from Wang *et al.*, 2012, and Chen *et al.*, 2014).

There have been some studies about the Chinshan-Shanchiao fault system, mainly on discussing the magnitudes of potential earthquakes on the fault system, possible inundation hazards in the Taipei basin induced by reactivation of the fault, and ground motion simulation of certain scenario based on kinematic source models. Wang *et al.* [2007] point out that the magnitudes of the potential earthquakes would be different based on where the earthquake nucleates and how many segments could break. Their research show that the possible values for the moment magnitude of the single Shanchiao fault rupture is $M_w = 6.6$, for the single Chinshan fault rupture is $M_w = 6.7$, and for the entire

Chinshan-Shanchiao fault system rupture is M_w = 7.0. The moment magnitude is less than 7.0 when the two faults break individually and could reach up to 7.0 when they fail simultaneously. Lai *et al*. [2008] use a dislocation model to model the Shanchiao fault rupture. They conclude that the Earth's surface would sink over 1.0 meters when an earthquake of M_w=6.5 happens, and over 2.1 meters down when an earthquake of M_w=7.0 happens. An extreme scenario could affect areas of Beitou, Guandu, Luzhou, Wugu, Taishan and Xinzhuang in the Taipei metropolitan area, the Earth's surface could sink beneath the sea level. Moreover, the magnitude exceeding M_w 7.0 could be as high as 64% [Wang and Kuo-Chen 2015]. In the next 50 and 100 years, the probability of recurrence of the next Shanchiao earthquake is estimated around 8.3% and 17.4%, respectively [Xu and Wang, 2017].

Chen *et al*. [2014] and Wang [2012] found out that the Chinshan-Shanchiao fault is a complex fault system with multiple bends: two bends along strike and one bend along down-dip. Nonplanar structure of the fault is very important in explaining observed seismograms, as shown by Sekiguchi *et al*. [1996] and Yoshida *et al*. [1996]. They determine the orientation of several fault segments as well as potential slip distributions. Aochi [2002] simulates the rupture process of the 1992 Landers earthquake, California using a realistic nonplanar fault geometry and compares the ground motion with observations. Although the synthetic seismic waves did not match the observational data well, they do show major characteristic features. Also, the results indicate the earthquake generation and ground motion are significantly affected by fault geometric complexity. Oglesby [2008] performs three-dimensional spontaneous dynamic rupture models of

potential earthquakes on the North Anatolian fault zone (NAFZ) under the Marmara Sea. The fault has multiple kinks. The study shows that earthquakes with hypocenters near the stepovers could hardly rupture the entire fault while with hypocenters far away from the stepovers could easily generate large through-going ruptures. Aochi [2005] suggests dynamic rupture process could be affected by the initial conditions on a fault system with different orientations. We try to understand how a rupture would propagate on the Chinshan-Shanchiao fault and how it is affected by initial conditions. The difference in the rupture process necessarily leads to differences in seismic-wave generation [Aochi, 2001]. So, we not only study the ground motion results due to the complexity of the fault system, but also test different models based on nucleation locations and initial conditions to explore possible ground shaking levels at important locations from various scenarios.

There is a case study about the ground motion simulation from potential earthquakes on the Chinshan-Shanchiao fault system. Wang [2012] simulates ground motion from three cases with different hypocenters. For example, there is a very strong directivity effect and near-fault effect that influence the velocity pulses as well as permanent displacement in synthetic waveforms. Furthermore, the waveforms in strike-normal components usually have larger amplitude than strike-parallel components in regions close to the fault. However, their study only considered three cases of earthquakes based on the different locations of hypocenters along strike direction, but the different locations along dip direction were not considered. It adopts the kinematic models of Irikura *et al*. [2010] to predict the strong ground motion. Kinematic models may overpredict the ground motion due to the coherent rupture fronts caused by assigned

rupture velocity [Olsen *et al*., 2008]. Therefore, we use EQdyna to simulate dynamic ruptures and ground motion, in which rupture velocity is part of the solution and with 3D velocity structures, the ground motion levels may be more realistic.

4.2. Methods and Models

We use FEM EQdyna to simulate earthquake dynamic rupture and wave propagation. The spontaneous rupture model needs fault geometry, material properties, initial stress field, and the friction law that governs the entire rupture propagation process.

4.2.1. Model description

We build a 3D Cartesian coordinate system choosing the epicenter of one of several models: (25.12° N, 120.76° E) as the origin. The fault-strike direction is x-axis, the fault-trace-normal direction is y-axis, and the vertical direction is z-axis. As the only active fault in north Taiwan, this fault system starts from the west edge of the Taipei basin, extending to the northeast direction, passes through the Tatun volcano group, and finally arrives at the Chinshan beach (Figure 4.1). The total length of the entire fault system could be over 74 km if the segment under the outer sea area were counted [Central Geological Survey, 2013]. But here we only consider the segments on and around the island which is around 50 km. We define the model length of the study area from -36 km to 84 km along x-axis, from -16 km to 104 km along y-axis, from -40 km to 0 km along z-axis, which does not only contain the fault geometry but also put the boundaries of the model far enough away from the fault to not contaminate the solutions on fault. Hexahedron

elements are used for the entire model. Element sizes are 0.2km, 0.2km and 0.089km along the x-axis, y axis and z axis, respectively. Wedges degenerated from hexahedrons are used to fit the dipping fault geometry.

4.2.2. Fault model

The complex fault geometry could affect the rupture propagation and ground motion. Many efforts have been made to characterize this active fault. The surface trace of the Shanchiao Fault was mapped [Chang *et al*., 1998; Lin *et al*., 2000; Lin, 2001; Huang *et al*., 2007; Chen, 2012; Y Want *et al*., 2012] close to the foothills of the Linkou Tableland and is subparallel to the Hsinchuang Fault. However, the exact fault trace on surface has yet been nailed down. Based on the information gathered from the papers above, we adopt two types of fault geometry along strike. We adopt the first type of model (we name it model M_0) as that the fault trace on surface is straight with strike 145° as shown in Figure 4.2. The second type (we name it model M_1) is based on the mapping from the studies above. The trace of the fault extends to about 50 km with a main strike of around 145° and two bends along strike. The first bend changes 20° of strike to the southeast and the second bend changes 10° of strike to the northeast. As for the vertical fault geometry, it is investigated for the first time by Chen *et al*. [2014] based on the basin-wide geological record of long-term tectonic subsidence since the Last Glacial Maximum (~23 ka). There is one bend with two fault segments along dip and the shallow segments dip to 75° while the deep segments dip to 15°. In summary, the fault has a total of six fault segments as shown in Figure 4.3. We name them sg1-sg6 accordingly. There are other eight models

named M2~M9 with the same fault geometry with model M_1 but with different initial stresses and friction coefficients that will be discussed later.

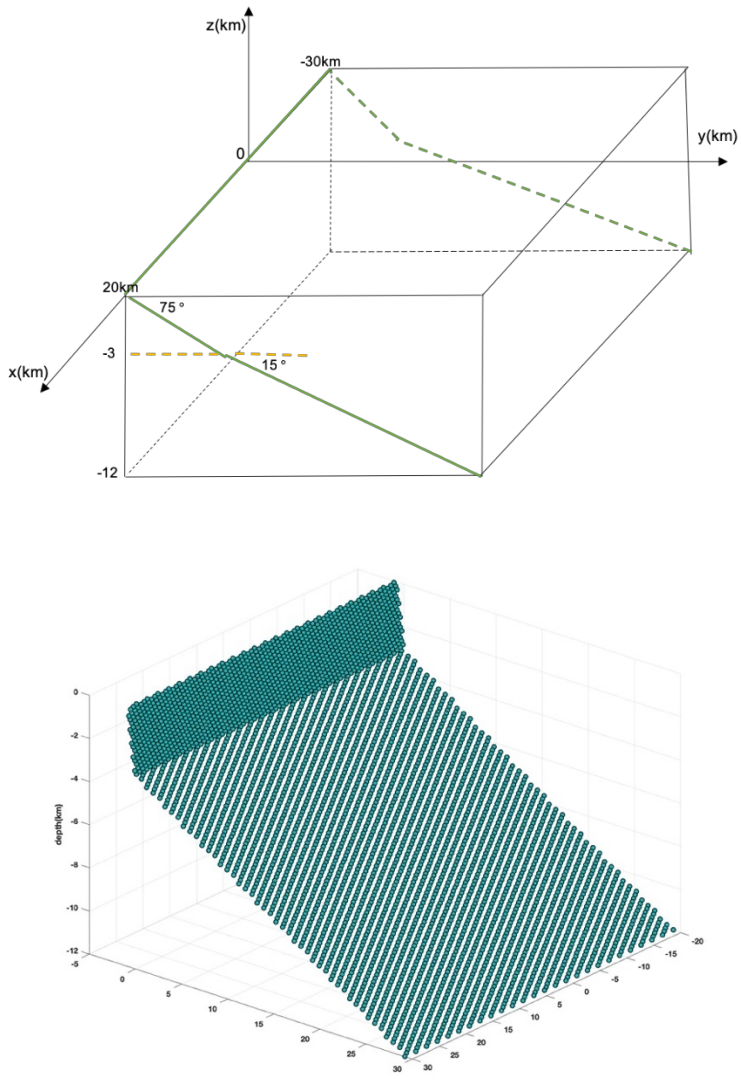

Figure 4.2. Fault geometry for M_0 without bending along strike. The fault strikes to 145° northeast with 50 km length.

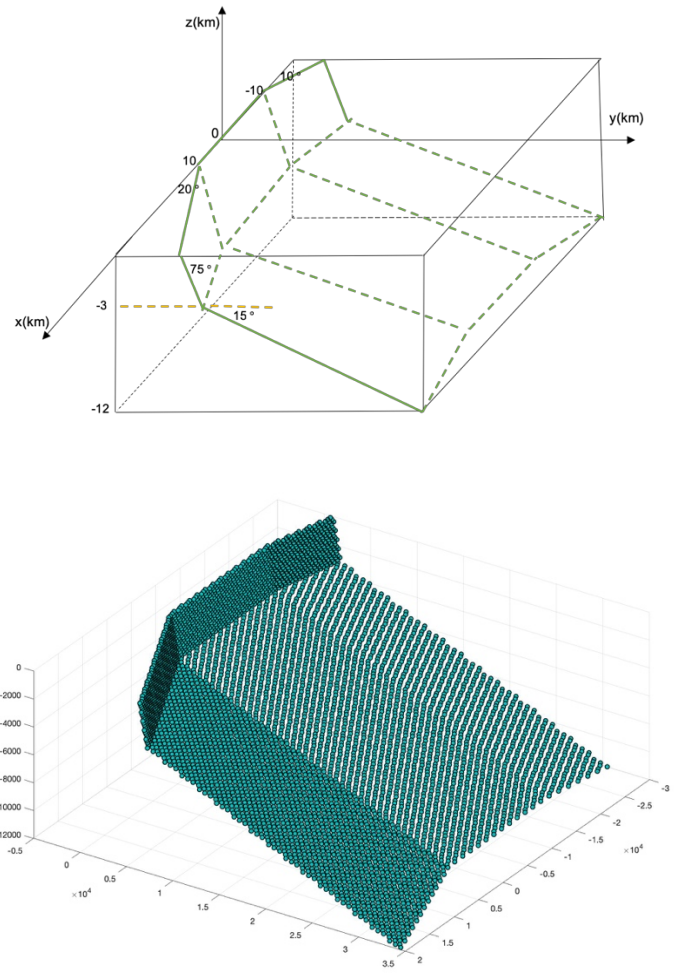

Figure 4.3. Chinshan-Shanchiao fault geometry from Model M_1 plotted in green solid and dashed lines in the Cartesian coordinate system. The positive x-axis points to southwest. The fault system contains six subsegments. The fault mainly strikes to 145° northeast with 20 km length. In south it extends another 20 km and bends 20° to southeast. In north it extends another 10 km and bends 10° to northeast. In the shallow part, the fault dips 75° from surface to -3 km depth and in the deeper part, it dips 15° from -3 km to -12 km depth.

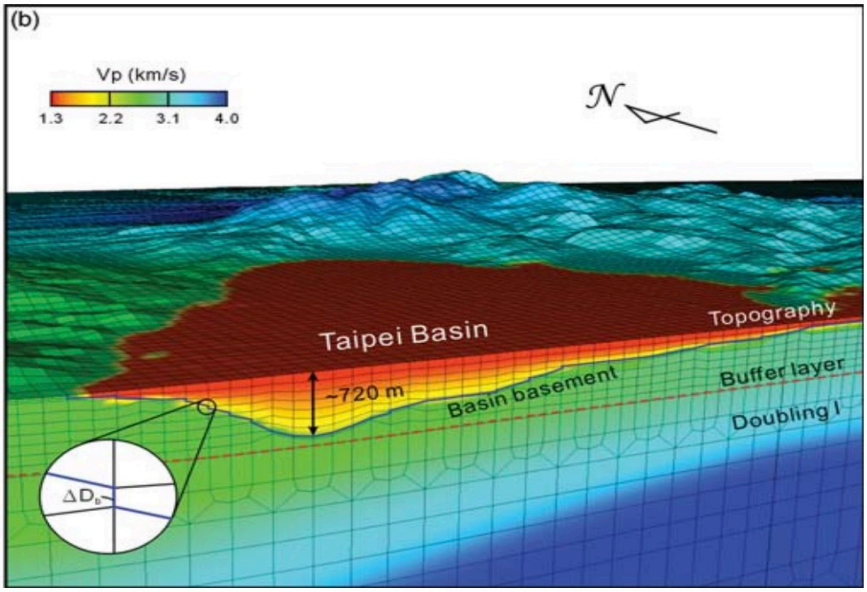

Figure 4.4. The grid model of Taipei basin [Lee *at al.*, 2008] The Taipei basin is a triangular-shaped basin. The southeast area is shallower than the northwest area. The colored parts present P wave velocity. The red part in the basin is around 1.3 km/s which is much slower than its surrounding areas.

4.2.3. Taipei basin and 3D velocity structure

The Taipei Metropolitan area is located on top of a triangular-shaped alluvium basin filled with the Quaternary unconsolidated sediments overlying the Tertiary basement. The sediments thicken northwestwards from a thin basin margin in the southeast to about 700 m in the northeast corner of the basin [Lin, 2001; Lee *at al.*, 2008]. Figure 4.4 shows the Taipei basin is a triangular-shaped basin. The P-wave velocity in the basin is lowest as 1.3km/s on the surface, which is much slower than its surrounding areas. Significant strong ground motion due to the amplification of low velocity sedimentary basin during an earthquake has been reported from many large earthquakes around the world, e.g., the 1989 Loma Prieta earthquake [e.g., Hough *et al.*, 1990], hypothetical earthquakes in

southern California [Olsen *et al*., 2008]. Previous analysis of site effect in the Taipei basin shows that high-amplification at low frequencies (0.2 – 1 Hz) and at high frequencies (1 – 3 Hz) can be correlated with the areas of deepest sediments and near the basin edges, respectively, except near a steep basin edge in the west [Wen and Peng, 1998]. In this model we apply a realistic 3D P-wave and S-wave velocity model [Huang *et al.*, 2014]. In Huang's model the interval along latitude and longitude is $0.08°$ and varied intervals along vertical direction with 0.5km, 2.5km, 3km, 4km and 5km. In this case study, we cut a cube out of the velocity model which covers the entire study area, extending from -50km to 40km in the fault's general strike direction, from -40km to 50km in the fault-normal direction, and from 0km to -40km in the vertical direction. In Figure 4.5 and 4.6, the P-wave and S-wave velocity at different depths in the study area are shown. In the figures, we could clearly see the distribution of the Taipei basin and the Sungshan sediment layer with smaller velocity than the surrounding area.

We interpolate the velocity structure to a grid with intervals of 200 m along longitude and latitude direction, and an interval of 61 m along vertical direction. Then, we load the velocity structures into EQdyna for simulations. The density calculation is shown in the equation (4-1), it is the same method as the equation (3-2). [Brocher *et al*.,2005]

$$\rho(g/cm^3) = 1.6612V_p - 0.4721V_p^2 + 0.0671V_p^3 - 0.0043V_p^4 + .000106V_p^5 \quad (4\text{-}1)$$

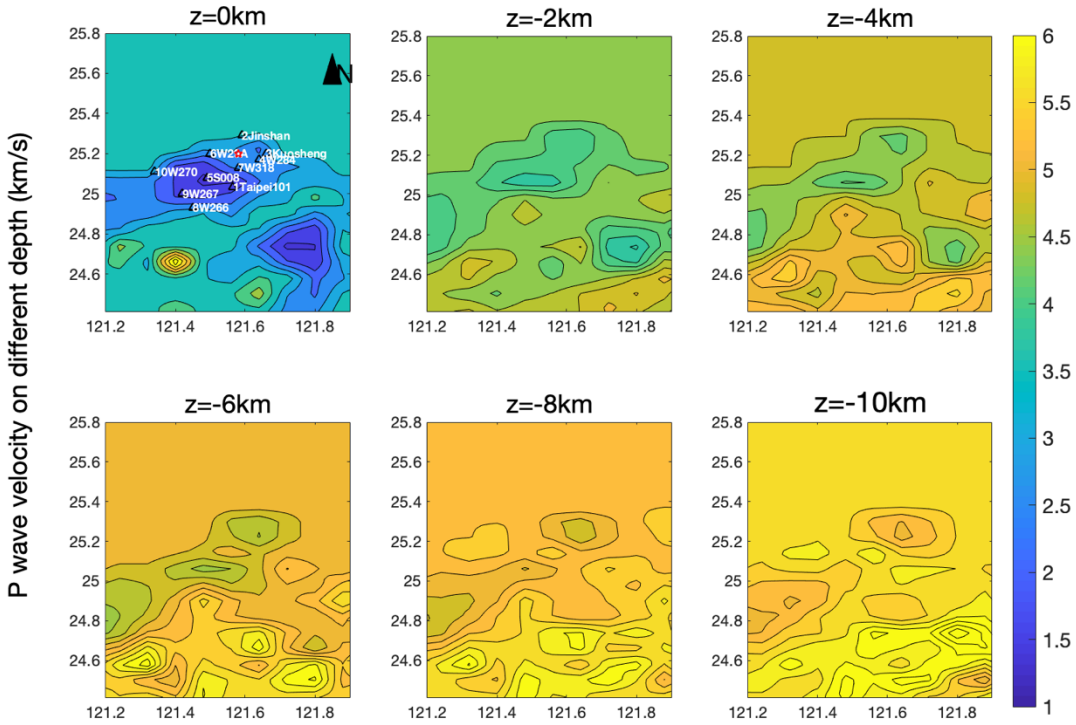

Figure 4.5. P wave velocity at different depths [Huang *et al.*, 2014]. z is the depth from the surface 0km to 10km. The depth step is 2 km. The velocity in the Taipei basin has the minimum velocity 1.38km/s.

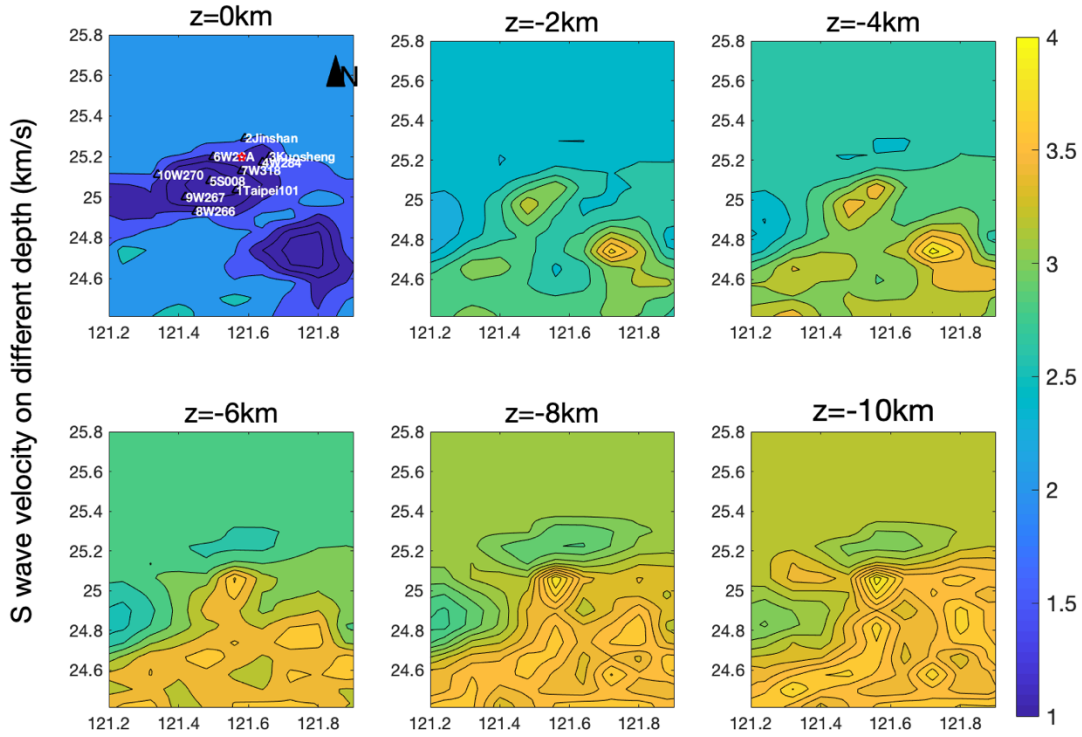

Figure 4.6. S wave velocity at different depths [Huang *et al.*, 2014]. z is the depth from the surface 0km to 12km. The depth step is 2 km. The velocity in the Taipei basin has the minimum velocity 0.24 km/s. In our model, we truncate the S wave velocity to minimum 0.5 km/s.

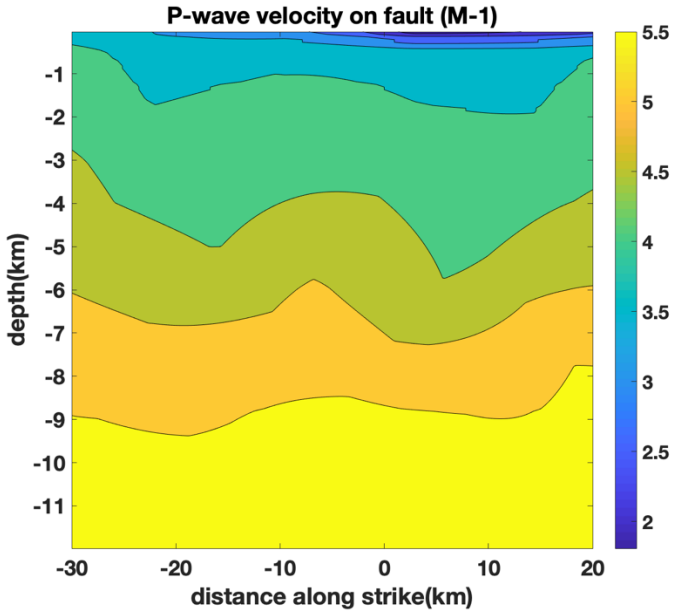

Figure 4.7. P-wave velocity on fault for model M_1. The dark blue area on top right shows the location of the Taipei basin. The unit of the velocity is km/s.

The velocity for the reference model M_R is chosen as a constant of 6.5 km/s. Figure 4.7 shows the P-wave velocity on the fault plane for M_0~M_9. The velocity range is from 2.1 km/s from the top to 5.8 km/s to the bottom. We could see the dark blue area on the top right of the plane is where the Taipei basin is located.

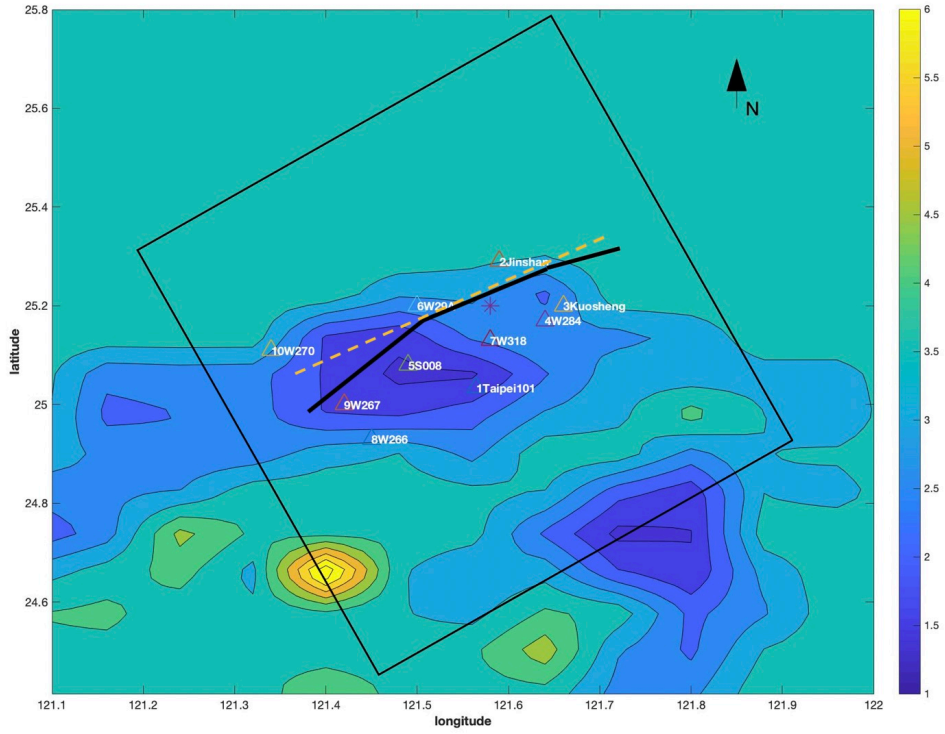

Figure 4.8. The yellow dashed line is the fault trace of M_0. The black solid curve line is the fault trace of M_1. The black square is the model area. The color triangles are the stations. The colors in the background are the P-wave velocity. The dark blue area near the fault traces is where the Taipei basin is located.

In Figure 4.8, we choose 10 stations from P-Alert strong motion network [Wu *el al.* 2013] to show the potential ground motion caused by different rupture scenarios. For example, we choose 1) Taipei101 building which is formerly known as the Taipei World Financial Center, 2) Jinshan and 3) Kuosheng as the two nuclear power plants. Among these stations, several of them are in the Taipei basin area, like 1Taipei101, 5S008, 9W267 while 7W318 is on the edge of the basin.

4.2.4. Friction law and choice of parameters

We use the slip-weakening law. In the law, the fault begins to rupture the fault begins to rupture when shear stress reaches to the shear strength. As the slip grows to the critical slip-weakening distance D_0, the frictional coefficient drops linearly from the static value μ_s to the dynamic value μ_d. Here we choose D_0 the critical slip distance as 0.3m.

Das and Aki [1977] defined a seismic S value, which is used to characterize how close the initial stress field is to the failure level. $S=(\sigma_u-\sigma_0)/(\sigma_0-\sigma_r)$, where σ_u is the strength, σ_0 is the initial stress, and σ_r is the sliding friction.

To initiate the spontaneous rupture, the rupture is forced to propagate at a fixed slow speed within an nucleation patch. Outside the nucleation patch, the rupture propagates spontaneously. It is important to estimate the size of the nucleation patch. Day (1982) assumes the crack is initially circular, and the circular crack initially expands uniformly, retaining circular shape. In Day's work, to estimate the critical radius r_c, Neuber's (1937) solution for the static slip on a circular shear crack in a Poisson solid is adopted.

$$s_\infty(r) = \frac{24}{7\pi}\frac{\Delta\tau}{\mu} r_c \sqrt{1-\frac{r^2}{r_c^2}} \qquad (4\text{-}2)$$

where s_∞ is the static slip, μ is the shear modulus, r_c is the crack radius, and r is the distance from the crack center. The total "available" energy, E, is defined as the drop-in strain energy due to crack formation minus the work done against friction, and can be calculated from the above equation.

$$\mathrm{E} = \frac{8\Delta\tau^2 r_c^3}{7\mu} \qquad (4\text{-}3)$$

The slip-weakening mechanism dissipates energy $\sum$ at the rupture front at the rate

$$\frac{d\sum}{dr_c} = \pi(S+1)d_0 r_c \Delta\tau \qquad (4\text{-}4)$$

per unit increase in crack radius. The desired estimate of the critical radius is r_c as in the following formula:

$$r_c = \frac{7\pi}{24}\frac{\mu(S+1)d_0}{\Delta\tau} \qquad (4\text{-}5)$$

where μ is the frictional coefficient. $\Delta\tau$ is the dynamic stress drop. $S = \frac{\tau_u - \tau_0}{\Delta\tau}$ is a measure of how near the initial stress field to failure is. For different models, the values of r_c are listed in Table 4.1 and Table 4.2.

To ensure numerical stability for the model, the dynamic simulation time step Δt, we calculate the time step as in the formula:

$$\Delta t = \alpha * dz/\max(Vp) = 0.003s \qquad (4\text{-}6)$$

where dz is the element size along vertical direction and max(Vp) is the maximum P wave velocity in the model. Here in the entire model, the max(Vp)=8.6km/s. α is between 0 to 1 as the coefficient and it is chosen as 0.5 here. To get waveforms at stations in the whole model area, the models simulate up to time t = 40s.

4.2.5. Initial stress setup

Initial stress fields on the fault surface play an important role to determine rupture propagations and earthquake magnitude. However, they may also be the least-constrained parameters. In this study, we compare different sets of initial stresses to observe how the rupture propagations and ground motions could be affected.

For the Chinshan-Shanchiao earthquake, it is a normal fault with some left-lateral strike-slip components. Three principal stresses σ_1 ,σ_2 and σ_3 are applied to the model where σ_1 is the vertical stress σ_z while σ_2 and σ_3 are the horizontal stresses. The direction of σ_1 is vertical, the largest horizontal stress σ_2 is along northeast direction, and the smallest horizontal stress σ_3 is along northwest direction. Here we let $\sigma_2 = \sigma_3$. Taking into account pore fluid pressure $p_f = \lambda\sigma_z = \lambda\rho gz$, where λ is the ratio between fluid pressure and lithostatic stress, we obtain the effective vertical principle stress σ_z is,

$$\sigma_z = \int(1-\lambda)\rho g dz \quad (4\text{-}7)$$

where ρ is the densities of rock and g is the gravity acceleration. In dry rock, $\lambda = 0$; while $\lambda \geq 0.9$ can be reached in water-saturated sediments. We choose a medium high value $\lambda = 0.6$ in this study.

According to Duan [2010], a stress ration R is defined by a nominal frictional coefficient μ_0 that characterizes the initial stress state on the fault plane

$$\mathrm{R} = \sigma_{max}/\sigma_{min} = [\sqrt{(1+\mu_0^2)} - \mu_0]^{-2} \qquad (4\text{-}8)$$

where σ_{max} and σ_{min} are the maximum and minimum principal stresses, respectively. The effective vertical stress σ_1 is the maximum stress σ_{max}, and the horizontal stresses σ_2 and σ_3 are set equally as σ_{min}.

For the choice of initial horizontal stress, static and dynamic friction coefficients, we compare several sets of different values as shown in Table 4.1 and get nine different models named from M_1-M_9. They are based on the average stress drop of 3 MPa. R is the ratio of the initial vertical stress and the minimum horizontal stress as in the equation (4-8). σ_z is the initial vertical stress from the equation (4-9) and σ_{h2} is the minimum

horizontal stress. μ_s is the static friction coefficient. μ_d is the dynamic friction coefficient. The initial shear stress is shown in Figure 4.9.

$$R = \sigma_z / \sigma_{h2} \qquad (4\text{-}9)$$

As mentioned before, nine models are built with different R and μ_s values while fix stress drop at 3Mpa to study how would these parameters affect the rupture propagation and ground motion. With different R values, the ratio between the vertical principal stress and the horizontal principal stress are different, which leads to different ratio (μ_0) of normal stress and shear stress, thus to keep fixed stress drop, the sliding friction coefficient μ_d will change correspondingly. We choose three different R values: 3.5, 3, 2.5 with fixed μ_s and three different μ_s values: 0.25, 0.3, 0.35 with fixed R values, therefore nine different models. Additionally, because the dipping angles at 0 km~-3 km deep and -3 km~-12 km deep are $75°$ and $15°$, respectively, μ_0 will be different on these fault segments. For the upper fault segments with steep dipping angle, μ_0 ranges from 0.4 to 0.6, but the μ_0 on the lower fault segments are much smaller, ranging from 0.18 to 0.21. Hence, the chosen μ_s with maximum value 0.35 will cause the upper fault segments fail easily. Based on this consideration and μ_0 is calculated as 0.4, 0.5, and 0.6, we choose larger μ_s values for upper fault segments accordingly. To keep a fixed shear strength for the upper fault, the μ_s are chosen as 0.6, 0.7 and 0.8, respectively. These parameters are shown in Table 4.1.

To evaluate the Taipei basin's effect on the ground motion, we choose a reference model M_R with homogeneous P wave velocity of 6.5 km/s and homogeneous vertical principal stress. For the reference model M_R and the model M_0 with no bend along

strike, shown in Table 4.2, we choose the same parameters, except the critical radius r_c, from the M_1 model in Table 4.1.

Table 4.1 Choice of model parameters for nine models

	M_1	**M_2**	**M_3**	**M_4**	**M_5**	**M_6**	**M_7**	**M_8**	**M_9**
R	3.5	3.5	3.5	3.0	3	3	2.5	2.5	2.5
$\boldsymbol{\mu_s}$	0.25	0.3	0.35	0.25	0.3	0.35	0.25	0.3	0.35
$\boldsymbol{\mu_0}$	0.21	0.21	0.21	0.2	0.2	0.2	0.18	0.18	0.18
$\boldsymbol{\mu_d}$	0.15	0.15	0.15	0.14	0.14	0.14	0.12	0.12	0.12
$\boldsymbol{r_c}$ **(km)**	4	6	8	5	7	9	7	8	10

Table 4.2 Choice of parameters for the model M_R and M_0

	M_R (homogeneous)	**M_0 (no kink)**
R	3.5	3.5
$\boldsymbol{\mu_s}$	0.25	0.25
$\boldsymbol{\mu_0}$	0.21	0.21
$\boldsymbol{\mu_d}$	0.15	0.15
$\boldsymbol{r_c}$ **(km)**	7	5

To resolve the normal and shear stresses on the fault, we firstly obtain traction vectors on the fault surface, then compute their dot products with unit vectors perpendicular and parallel to the fault, respectively. We calculate the unit normal vectors $\hat{\boldsymbol{n}}$, unit shear vectors along strike direction $\hat{\boldsymbol{s}}$ and along dip direction $\hat{\boldsymbol{d}}$ on the six fault segments sg1-sg6 as in Table 4.3.

Table 4.3 Three unit vectors on the six fault segments

	Normal Vector ($\hat{\boldsymbol{n}}$)	**Shear vector along strike ($\hat{\boldsymbol{s}}$)**	**Shear vector along dip ($\hat{\boldsymbol{d}}$)**
sg1	(-0.3317,0.9112,0.2442)	(-0.9397,-0.3420,0)	(-0.0835,0.2295,-0.9697)
sg2	(0.0,0.9659,0.2589)	(-1,0,0)	(0.0,0.2589,-0.9659)
sg3	(0.1679,0.9522,0.2551)	(-0.9848,0.1736,0)	(0.0443,0.2512,-0.9669)
sg4	(-0.1029,0.3024,0.9476)	(-0.9467,-0.3221,0)	(-0.3052,0.8971,-0.3194)
sg5	(0.0,0.2924,0.9563)	(-1,0,0)	(0.0,0.9563,-0.2924)
sg6	(0.0374,0.2949,0.9548)	(-0.9921,0.1258,0)	(0.1201,0.9472,-0.2973)

The traction $\mathbf{t}(\hat{\boldsymbol{n}})$ on the fault surface is calculated by multiplying the stress tensor by $\hat{\boldsymbol{n}}$, that is,

$$\mathbf{t}(\hat{\boldsymbol{n}}) = \boldsymbol{\tau}\hat{\boldsymbol{n}} = \begin{bmatrix} \boldsymbol{t_x}(\hat{\boldsymbol{n}}) \\ \boldsymbol{t_y}(\hat{\boldsymbol{n}}) \\ \boldsymbol{t_z}(\hat{\boldsymbol{n}}) \end{bmatrix} \quad (4\text{-}10)$$

To resolve the normal and shear stress on the fault, we compute the dot products with unit vectors perpendicular ($\hat{\boldsymbol{n}}$) and parallel ($\hat{\boldsymbol{s}}$) and ($\hat{\boldsymbol{d}}$) to the fault

$$\boldsymbol{\sigma_n} = \boldsymbol{t} \cdot \hat{\boldsymbol{n}} \quad (4\text{-}11)$$

$$\boldsymbol{\tau_s} = \boldsymbol{t} \cdot \hat{\boldsymbol{s}} \quad (4\text{-}12)$$

$$\boldsymbol{\tau_d} = \boldsymbol{t} \cdot \hat{\boldsymbol{d}} \quad (4\text{-}13)$$

$\boldsymbol{\sigma_n}$ is the normal stress on the fault plane, $\boldsymbol{\tau_s}$ is the shear stress along strike, $\boldsymbol{\tau_d}$ is another shear stress along dip.

Figure 4.9 shows the initial normal stress, shear stress, final shear stress and stress drop distribution for different models of M_R, M_0 and M_1. For M_R, the principle stresses are uniform in the research region, but the magnitude of the resolved fault stress components changes on six different segments due to the rotation of the two principal stress components. The stresses change dramatically between the upper and lower fault segments because of the large bending angle difference. The initial stresses for model M_0 are heterogeneous and depth-dependent. But without any kink along fault-strike direction, there is no obvious variations horizontally. The initial stresses for model M_1 are depth-dependent and heterogeneous, too. Note that the initial stresses on the upper fault for both M_R and M_1 change so little that they look like homogeneous because the values are

very small relative to lower faults. For the model M_R and M_1 the stress drop on the lower right fault segments are higher than the lower middle and left fault segments.

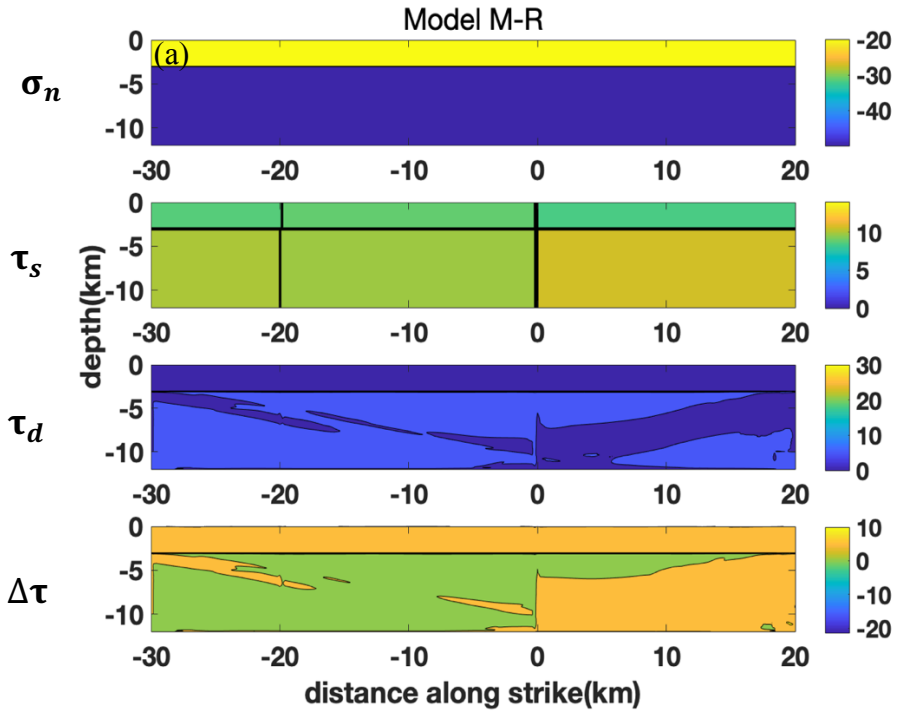

Figure 4.9. (a) Stress distribution on M_R; (b) stress distribution on M_0; (c) stress distribution on M_1. It shows the initial normal stress σ_n, shear stress τ_s, final shear stress τ_f and the stress drop $\Delta\tau$ on the fault planes of the three models M_R, M_0 and M_1. The unit of the stresses is MPa. (Figure 4.9b and 4.9c are continued on the next pages)

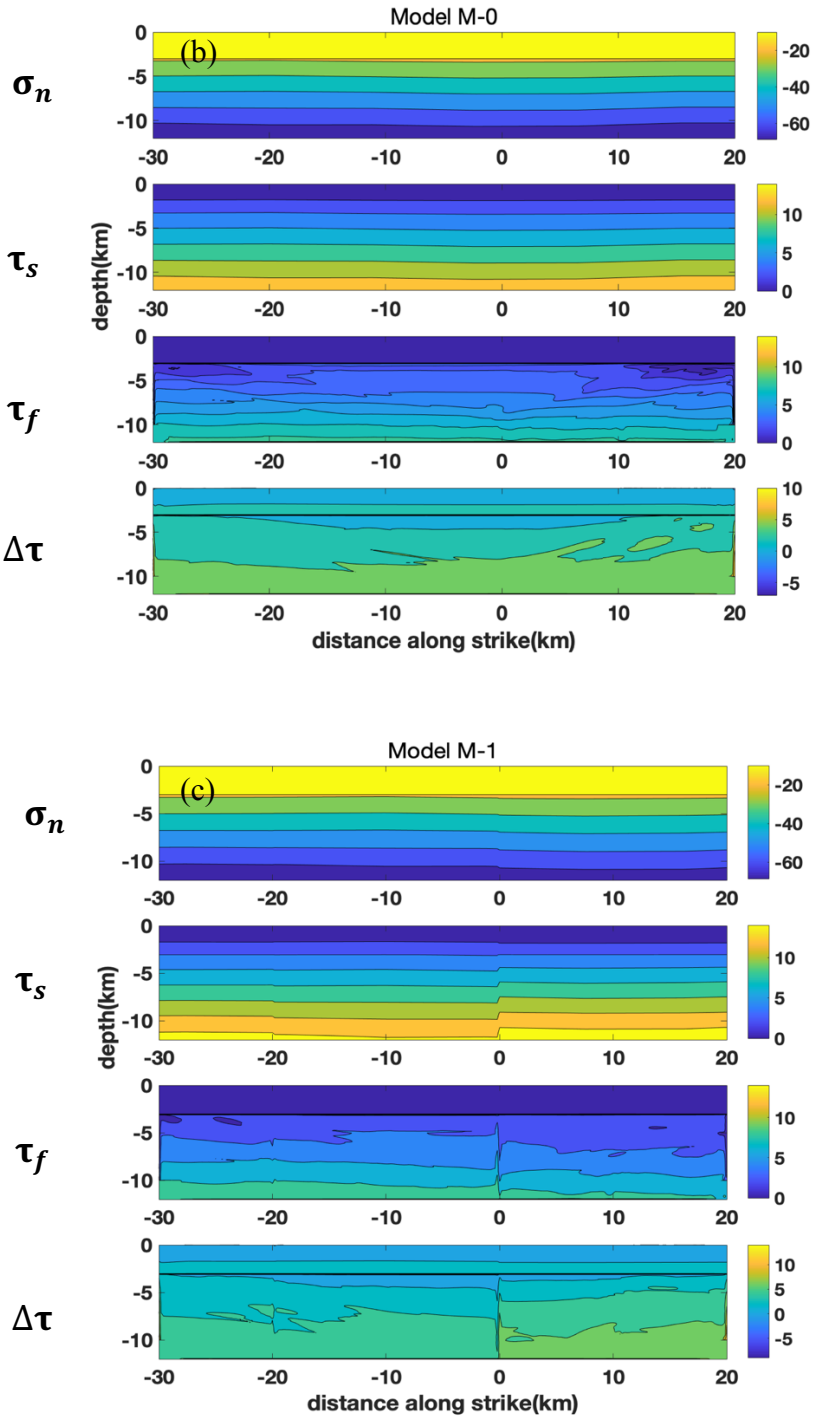

Figure 4.9. Continued.

4.3. Results and Analysis

4.3.1. Reference model results

The reference model M_R uses a homogeneous velocity model, with fault geometry with kinks along strike and dip direction. The hypocenter is in the middle of the fault segment 2. From Figure 4.10, we could see the rupture propagates smoothly except near the kink along the vertical direction at -3km depth. The rupture is delayed at this kink because of the large variation of the dipping angle. Just like in the slip distribution contour, the slips are very small near the kink compared to other places. On the other hand, the slips become larger starting from the kink at 0 km along strike. However, the slips at the other kink along strike at -20km do not show significant change. It is possibly because the angle near this kink is 10° smaller which does not cause as much influence as the 20° bend.

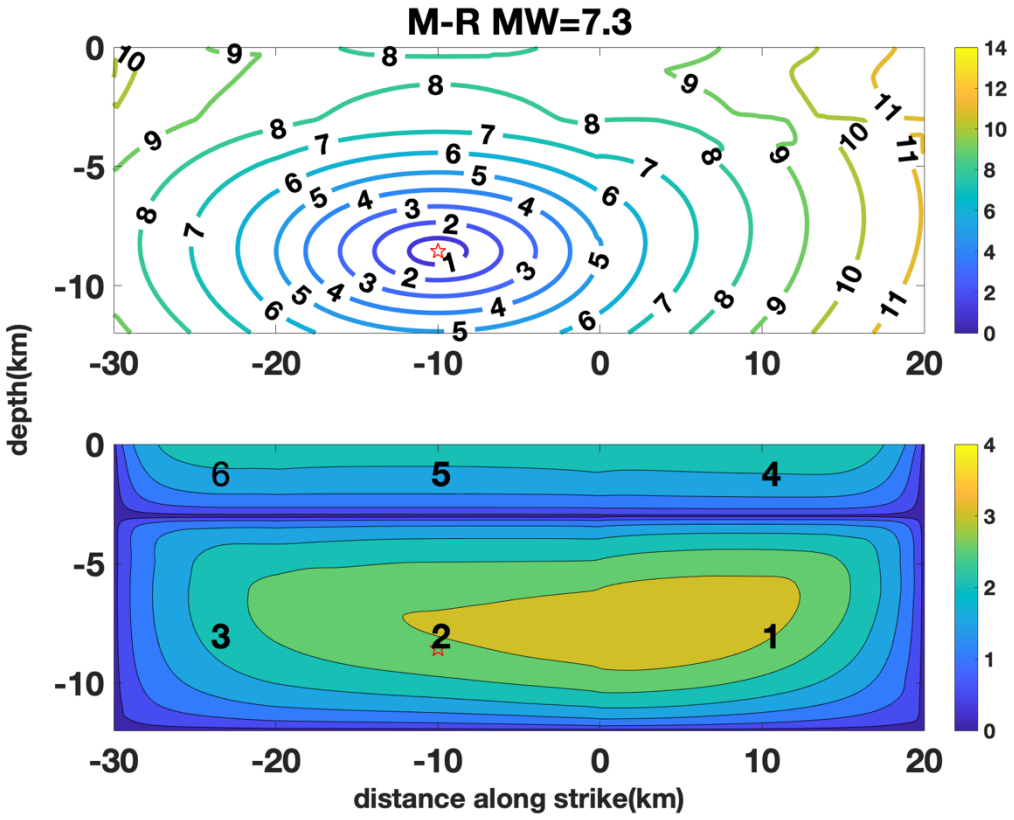

Figure 4.10. The rupture time and slip distribution on the fault plane for model M_R. The upper panel is the rupture time contour. The lower panel is the slip distribution on the fault. The red star is the hypocenter. The black numbers indicate the six fault segments.

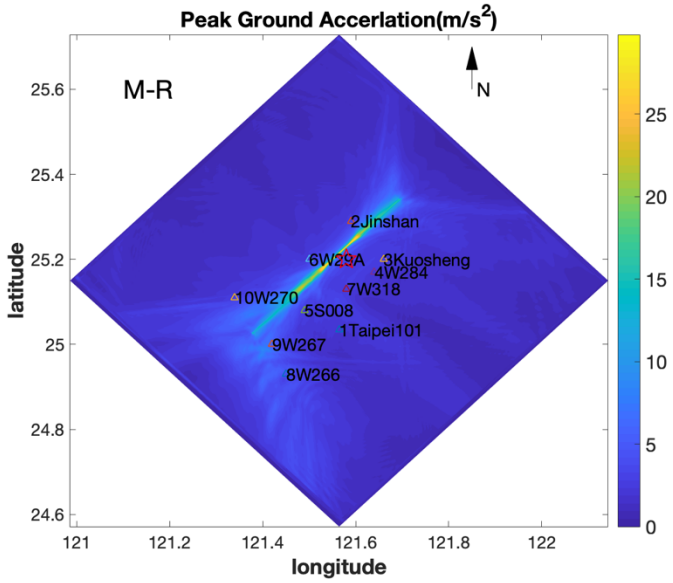

Figure 4.11. Peak ground acceleration on the surface for model M_R. The triangles are the chosen stations. The colors in the background show the magnitude of the PGA.

In Figure 4.11, the peak ground acceleration (PGA) distribution is mostly even extending from the epicenter to both sides along strike, except for locations near the larger kink where the PGA is a little larger.

4.3.2. Model (M_0) without kinks along strike results

This model has applied realistic velocity model and depth-dependent initial stress with no bending along strike. In Figure 4.12, compared to the model M_R, without bend along strike, the rupture time contour shows symmetric features on both sides of the hypocenter. The rupture reaches the left end of the fault at around t=9s and the right end of the fault at around t=12s. The upper fault starts breaking at t=7s. We could see more details in the slip distribution because of the realistic velocity distribution. Different than

the reference model M_R in which the slip contour in the upper fault segments are smooth, the fault segment 4 has larger area with high slip values than the fault segment 5 and 6, which may be caused by the low-velocity basin effect at the shallow depth.

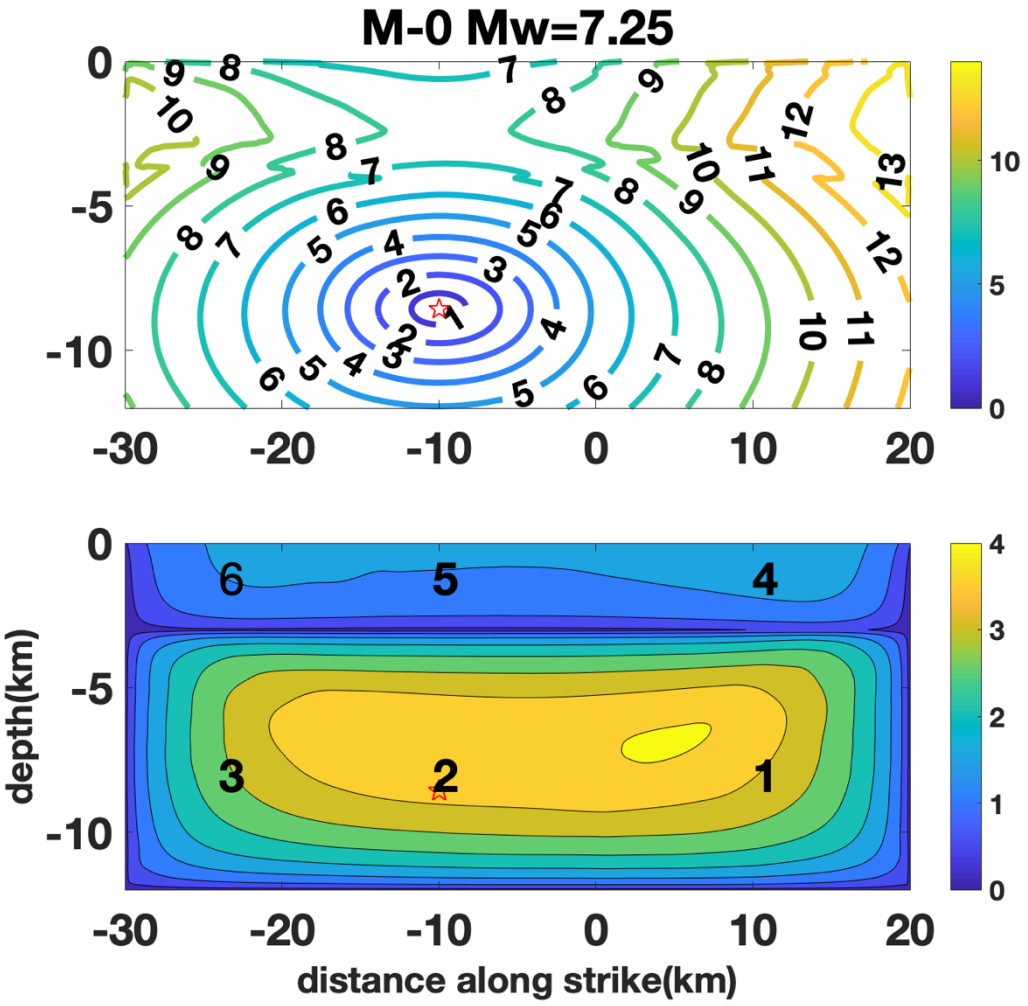

Figure 4.12. The rupture time and slip distribution on the fault plane for model M_0. The upper figure is the rupture time contour. The lower figure is the slip distribution on the fault. The red star is the hypocenter. The black numbers indicate the six fault segments.

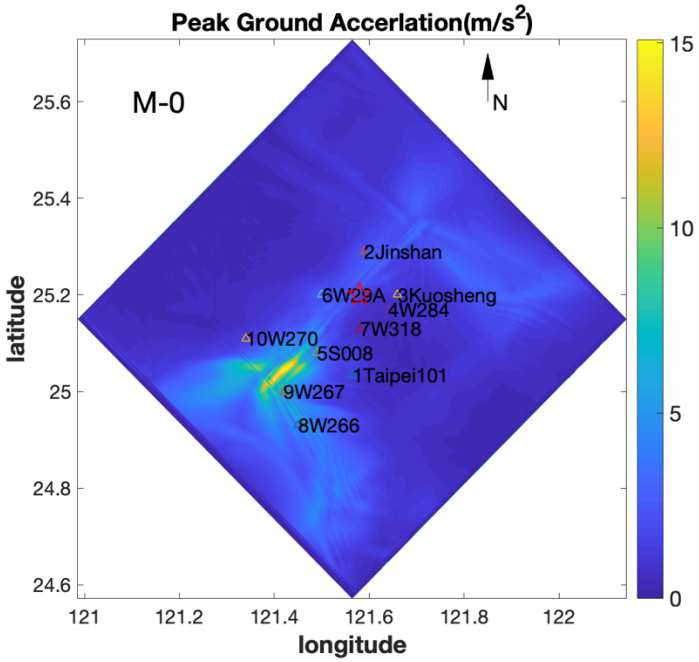

Figure 4.13. Peak ground acceleration on the surface for model M_0. The colored triangles are the chosen stations. The yellow and blue colors in the background show the magnitude of the PGA.

The PGA plot in Figure 4.13 for model M_0 shows significantly large accelerations near west of the Taipei basin area (near 5S008) which are amplified because of the low shear wave velocity of the soft Songshan deposit layer on the top of the basin.

4.3.3. Model (M_1 to M_9) results

Model M_1 has the highest R (3.5) value and lowest μ_s (0.25) value. Figure 4.14 shows horizontal and down-dip slip and slip-rate in the left figure and the stress evolution in the right figure along strike, dip and normal direction, respectively, on one of the on-fault stations near the hypocenter. From the left figure of particle movement, we could see

there is not only vertical velocity and slip downwards, but also along the strike direction. The right figure shows the vertical stress increase to strength first, then decrease 3 MPa to the sliding friction.

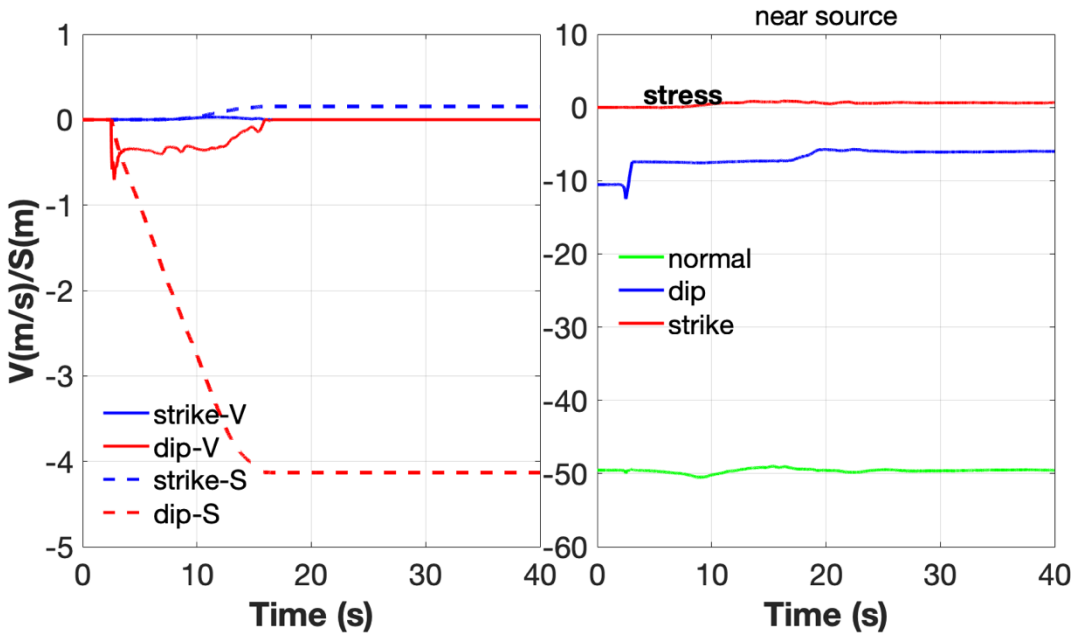

Figure 4.14. On-fault station velocity, slip and stress history for model M_1. The left figure is the velocity and slip history along dip and strike direction. The right figure is the stress history along three directions.

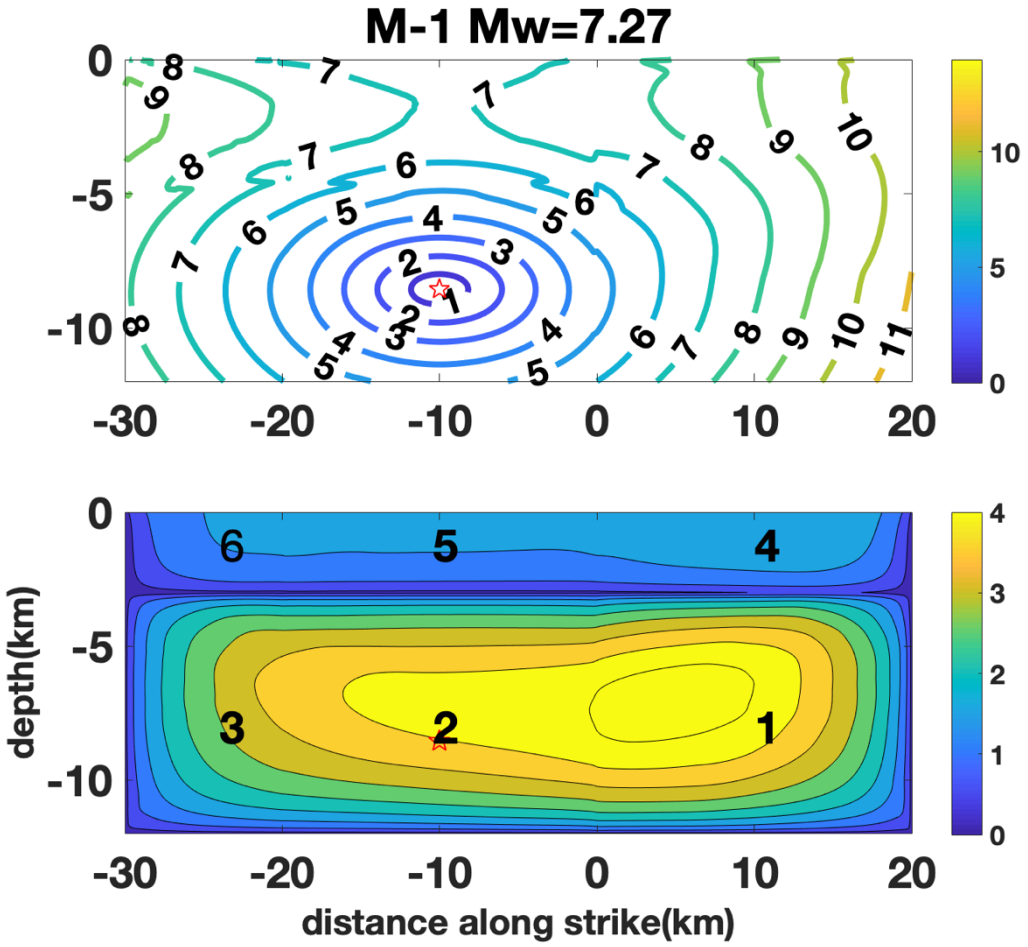

Figure 4.15. The rupture time and slip distribution on the fault plane for model M_1. The upper figure is the rupture time contour. The lower figure is the slip distribution on the fault. The red star is the hypocenter. The black numbers indicate the six fault segments.

Figure 4.15 shows the rupture time and slip distribution on the fault plane for the model M_1. In the rupture time contour, the rupture reaches the left end of the fault at t=8 s and the right end at t=11 s. Note that the rupture in the model M_0 without kink along fault-strike, the rupture reaches the left end at t=9 s and right end at t=12 s. The rupture propagates faster in the model M_1 than in the model M_0. Unlike the kink along the dip direction which has arrested the rupture propagation, the rupture is facilitated by the stress

condition due to the kink along the strike. In the slip distribution figure, the highlighted yellow area has the highest slip values ranging from 4.2m to 4.7m which are larger than the slip in the model M_0.

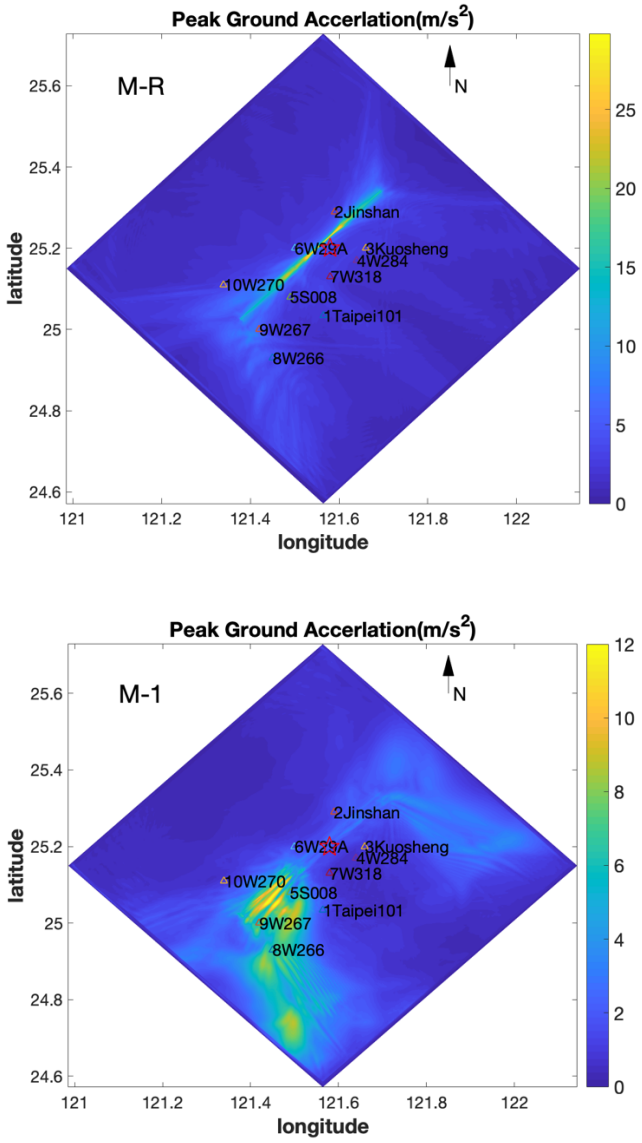

Figure 4.16. Comparison of the peak ground acceleration between the models M_R and M_1. The upper figure is the PGA on surface in the reference model M_R. The lower figure is the realistic model M_1. The stations are shown in the figure.

In Figure 4.16, comparing the two models of the reference model M_R and the model M_1 with realistic material properties, in the model M_R the PGA distribution is approximately symmetric on the two sides of the epicenter along the fault, while in the model M_1 PGA is amplified towards the Taipei basin area due to low shear wave velocity.

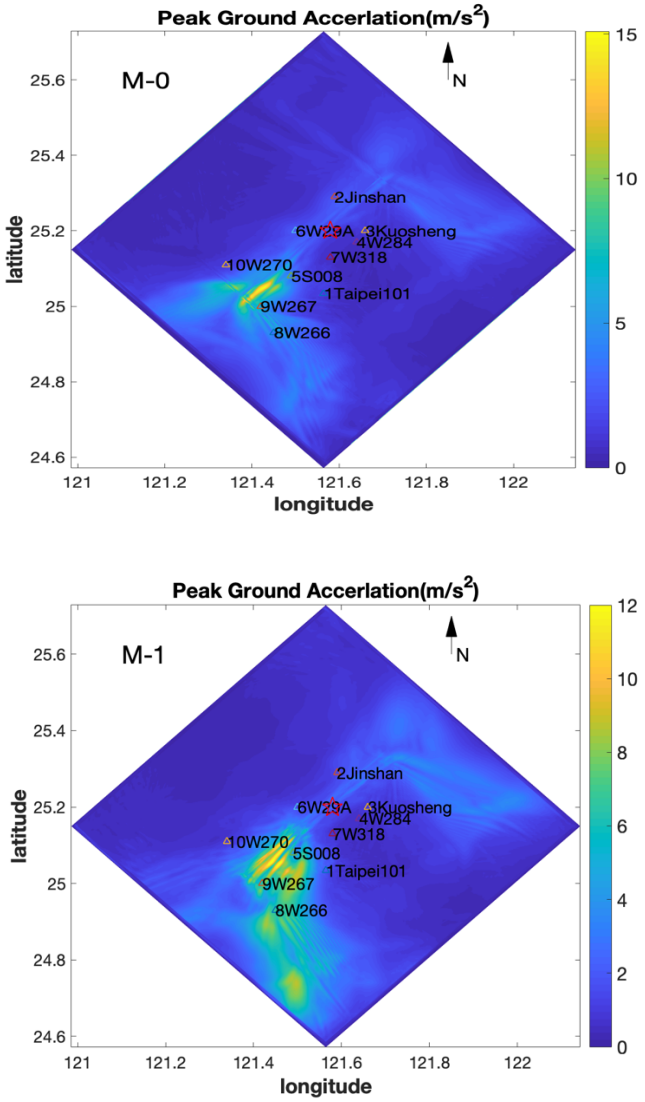

Figure 4.17. The upper figure is the PGA distribution in the model M_0. The lower figure is the PGA distribution in model M_1 with realistic 3D velocity structure.

In Figure 4.17 comparing the model M_0 without kink along strike and the M_1 with kinks along strike. We could clearly see the PGA is affected by the bent fault geometry and the Taipei basin.

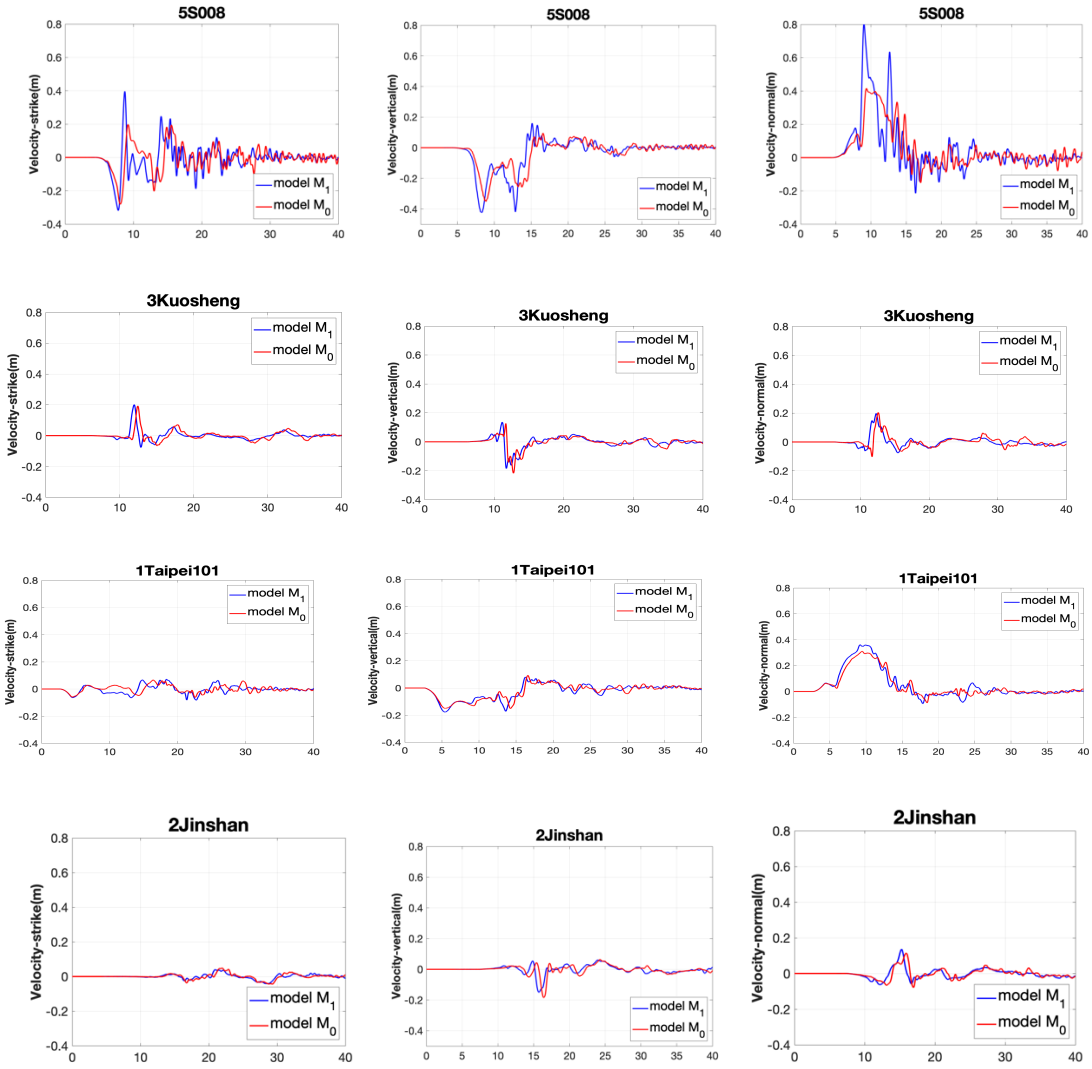

Figure 4.18. Particle velocity (m/s) comparison of two models with different fault geometries, M_0 and M_1, along fault-parallel, vertical and fault-normal directions. The left column figures show the fault-parallel component, the middle column figures show the vertical component, and the right column figures show the fault-normal components.

Figure 4.18. Continued.

Figure 4.18 shows the three components of the peak ground velocity (PGV) history comparison between the two models of M_0 and M_1 for five different off-fault stations. Among these stations, 1Taipei101, 5S008, and 9W267 are either in the basin or on the edge of the basin, while 2Jinshan and 3Kuosheng are far from the basin in the north of the study area. Clearly, we could see the magnitude of the peak ground velocity of the stations 1Taipei101, 5S008, 9W267 are larger than other two stations because of the basin amplification. Also, the durations of the movements of these stations are longer than others. Comparing the results of different models M_0 and M_1, the arrival of the wave in M_1 is slightly earlier than M_0 and the magnitude of the velocities are obviously larger in M_1 than in M_0, which may be caused by the kink along the strike direction and the variation of the orientation of the stress field.

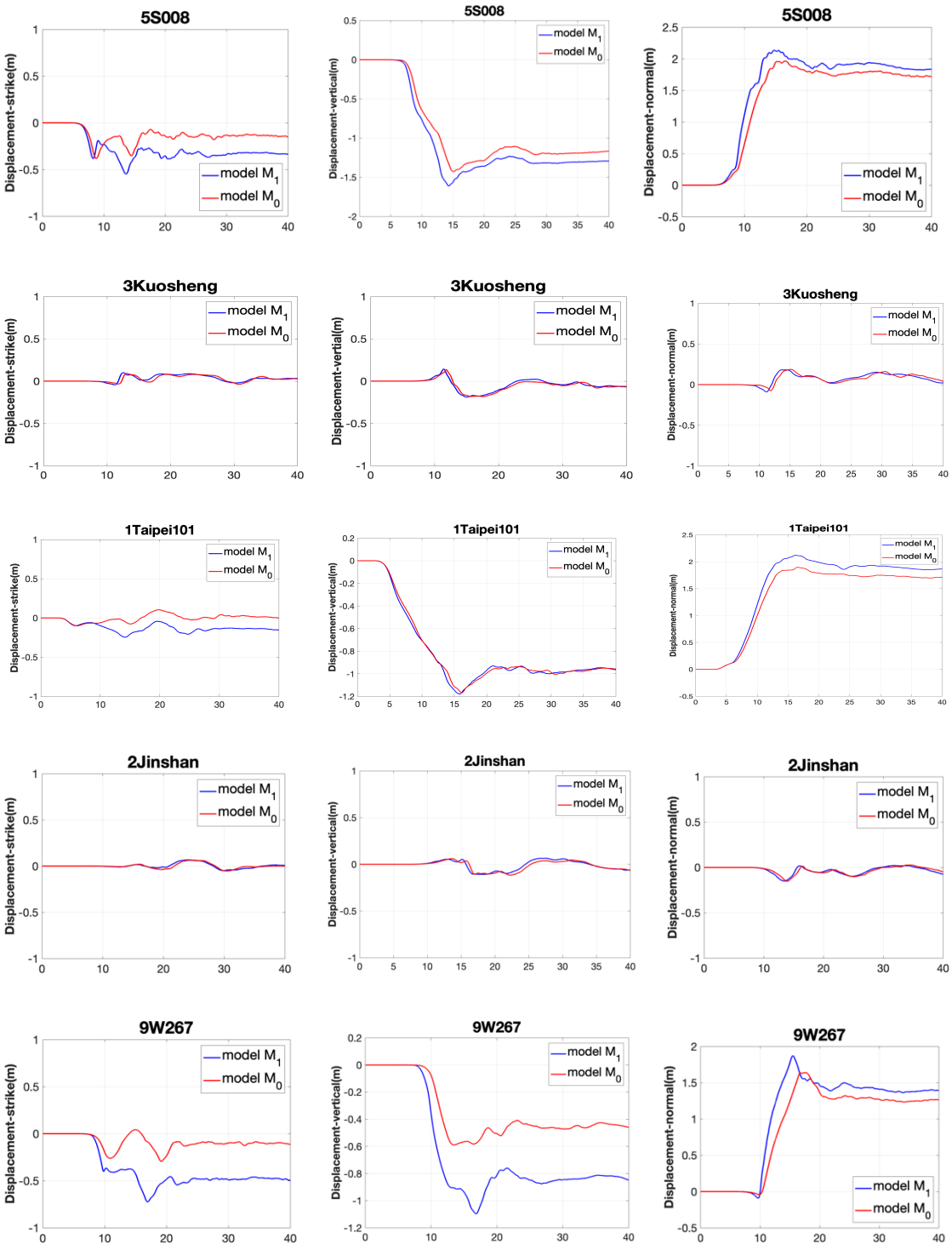

Figure 4.19. Particle displacement comparison of two models M_0 and M_1 along fault-parallel, vertical and fault-normal directions at several stations.

In Figure 4.19 the displacement history of the five stations for two models M_0 and M_1 are compared. Similar to the peak ground velocity comparison in Figure 4.18, the magnitude of the displacement for the model M_1 are apparently larger than the model M_0. Also, the displacement in the stations of 1Taipei101, 3Kuosheng and 5S008 are permanent and could subside 2m.

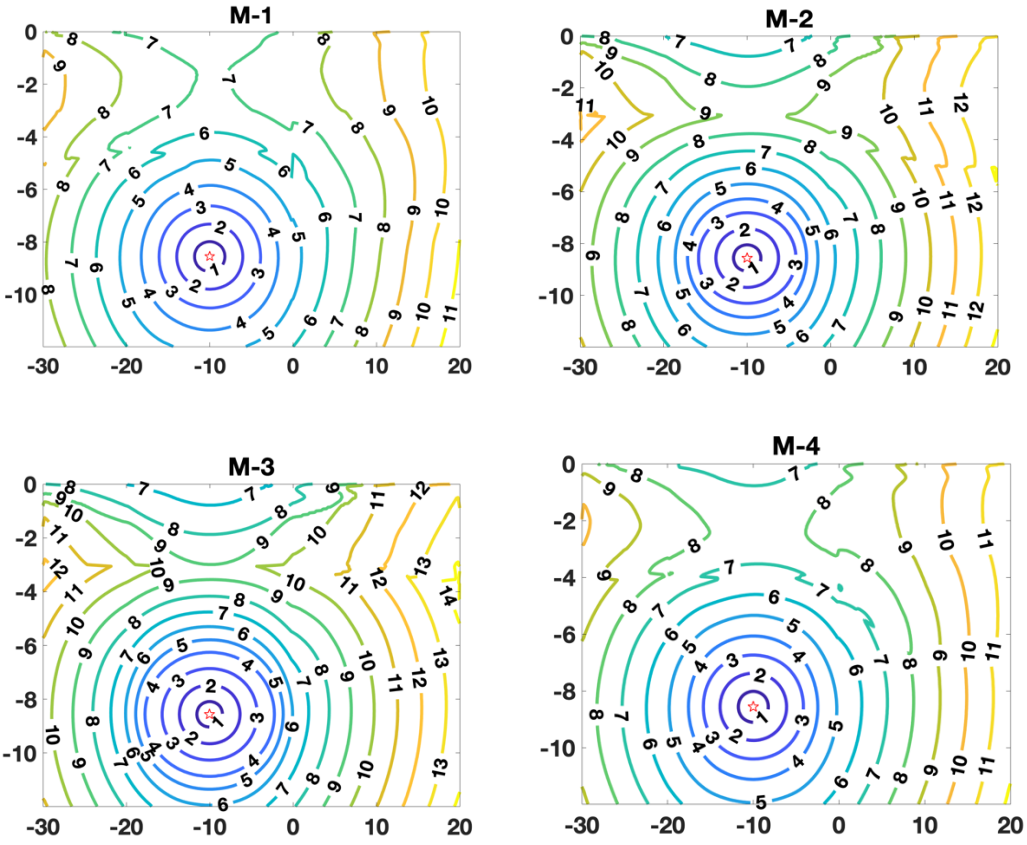

Figure 4.20. The rupture times on the fault plane for model M_1 to M_9. The red star is the hypocenter. The horizontal axis is the distance along strike (km). The vertical axis is the depth (km).

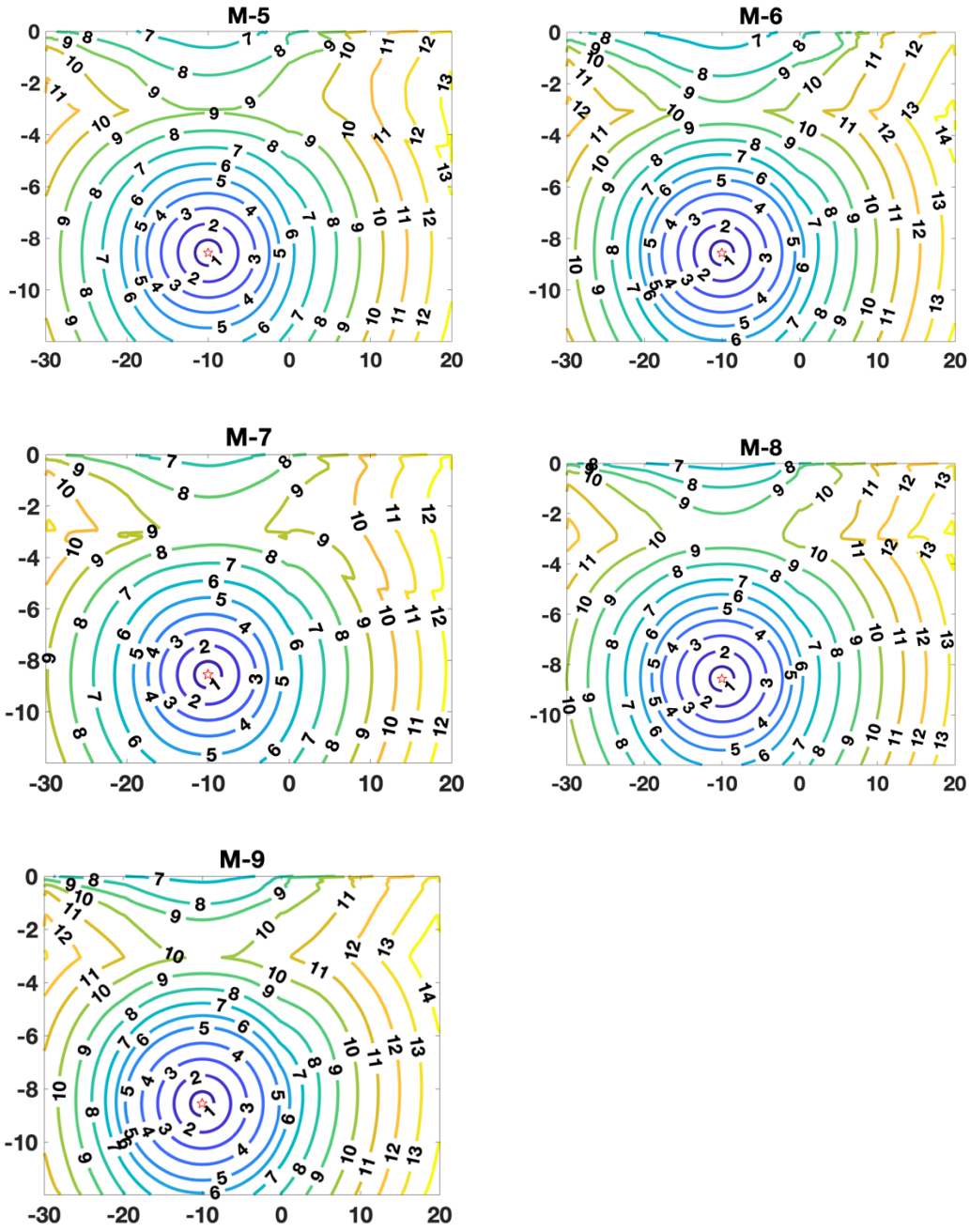

Figure 4.20. Continued.

Below we compare dynamic ruptures of Model M_1 to M_9. To study the results in Figure 4.20, firstly, compare the first three models from M_1 to M_3. With a fixed R

value and variable $\boldsymbol{\mu_s}$ as 0.25, 0.3 and 0.35. From the first three subplots, we can see that, the rupture time increases as $\boldsymbol{\mu_s}$ increases. For example, in the model M_1, the rupture reaches to 20km along strike at around 10s, 12s for the model M_2, and 14s for the model M_3. Similarly, for the other two sets of M_4 to M_6 and M_7 to M_9 the same feature shows in the figures. This may be because as μ_s increases, with a fixed stress drop and a shared initial friction coefficient, the S value, which represent how the rock is close to failure, also increases. The larger S values, the more difficult the rupture is to propagate. Then we compare M_1, M_4 and M_7, the rupture time contour shows the same feature as the R value decreases. The rupture propagates to 20km at around t=11s in M_4, and t=12s in M_7. It means, for a normal fault, as the ratio between the vertical principal stress and the minimum horizontal principal stress decreases, the rupture is more difficult to propagate.

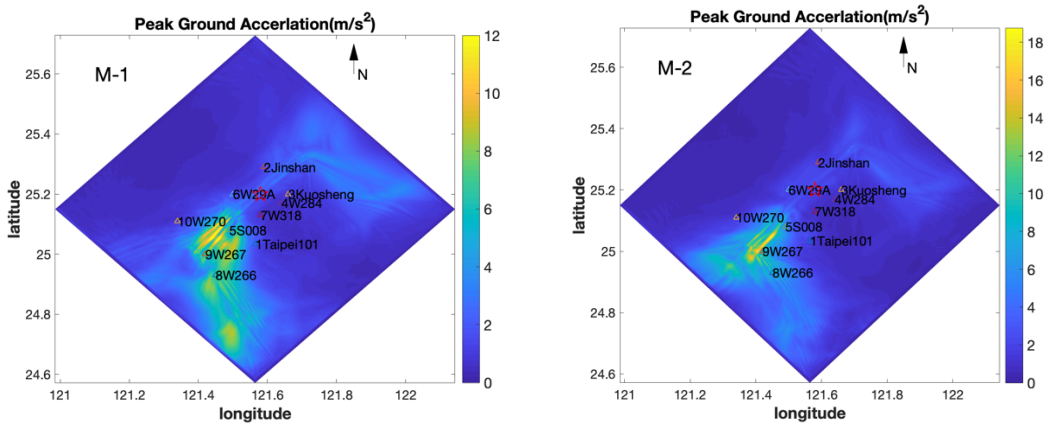

Figure 4.21. Peak ground acceleration on the surface for model M_1 to M_9. The colored triangles are the chosen stations. The yellow and blue colors in the background show the magnitude of the PGA.

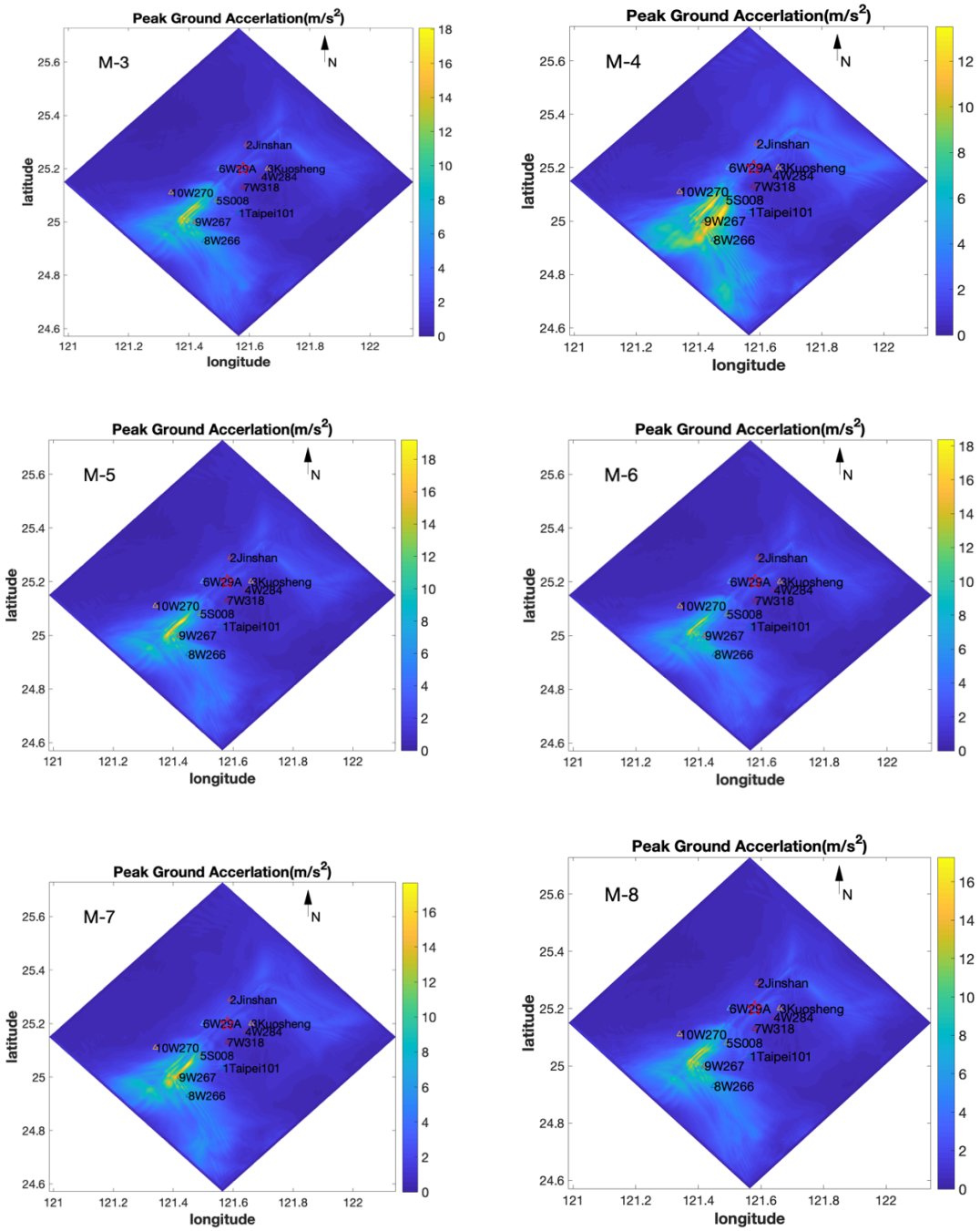

Figure 4.21. Continued.

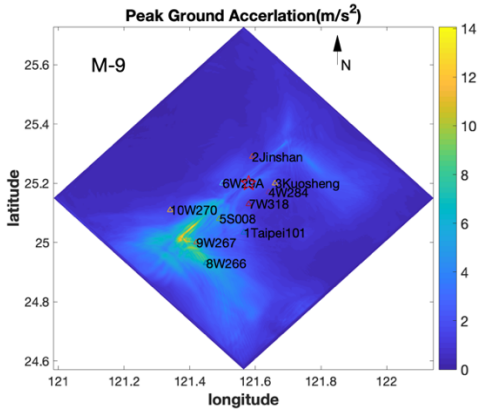

Figure 4.21. Continued.

Figure 4.21 show PGA distributions of M_1 to M_9. One common feature is the strong basin effect on PGAs due to the low rigidity of the low-velocity sedimentary basin in the southeast. For near-fault PGAs, they are large in southeast portion due to the combination of basin effect and rupture directivity effect. For PGAs at stations off the fault, Stations 5S008 and 9W267 show basin-induced amplification. However, the PGAs east of the basin are relatively smaller, like at Station 1Taipei101. This effect appears to be related to the shape of the basin because the depth in the west is around 720 m and it decreases as the basin extends to the east.

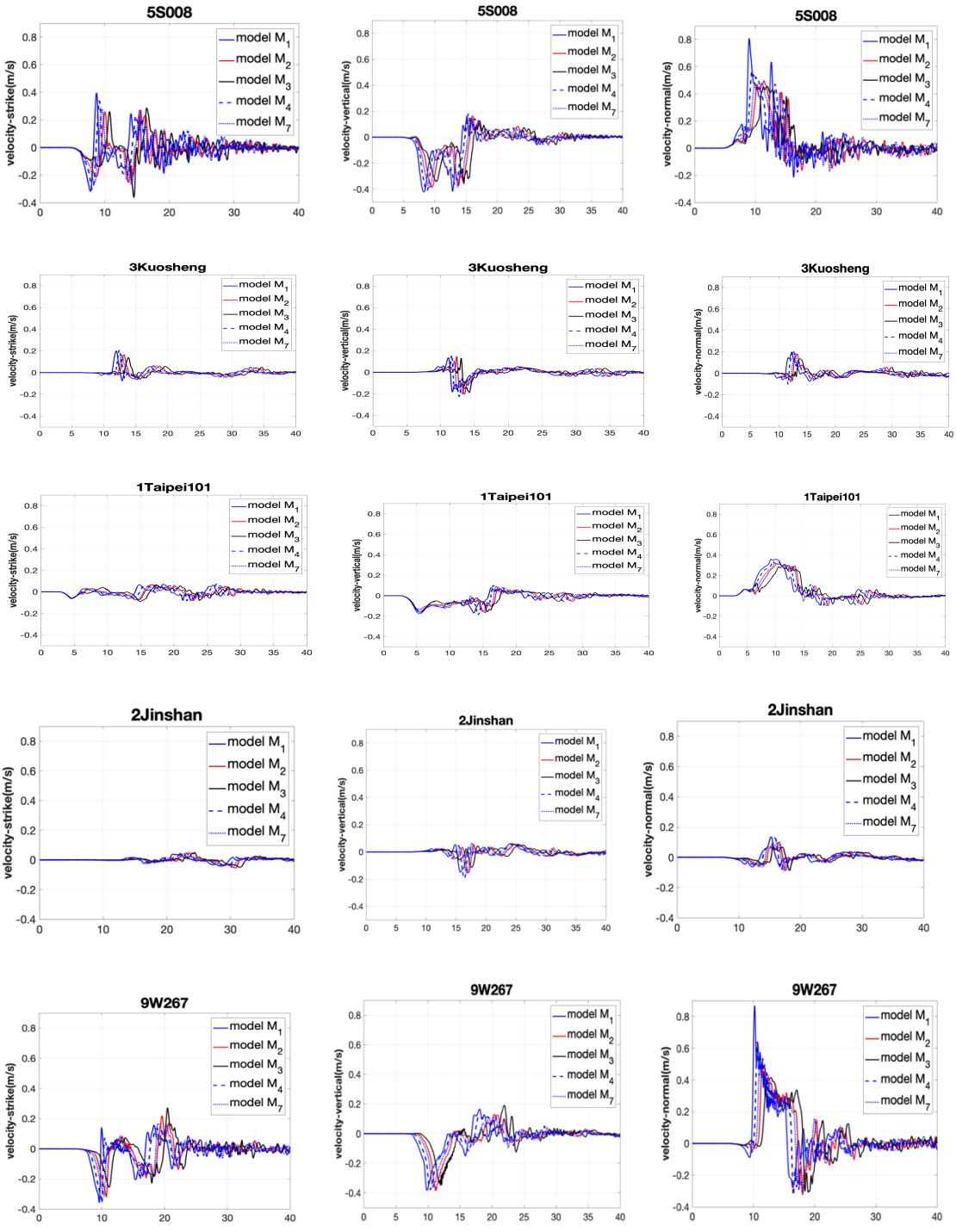

Figure 4.22. Simulated particle velocity history on the off-fault stations 1Taipei101, 2Jinshan, 3Kuosheng, 5S008, and 9W267 from P-alert network. The x-axis is the time (sec), and the y-axis is the peak ground velocity (m/s). Five models are plotted as in the figures.

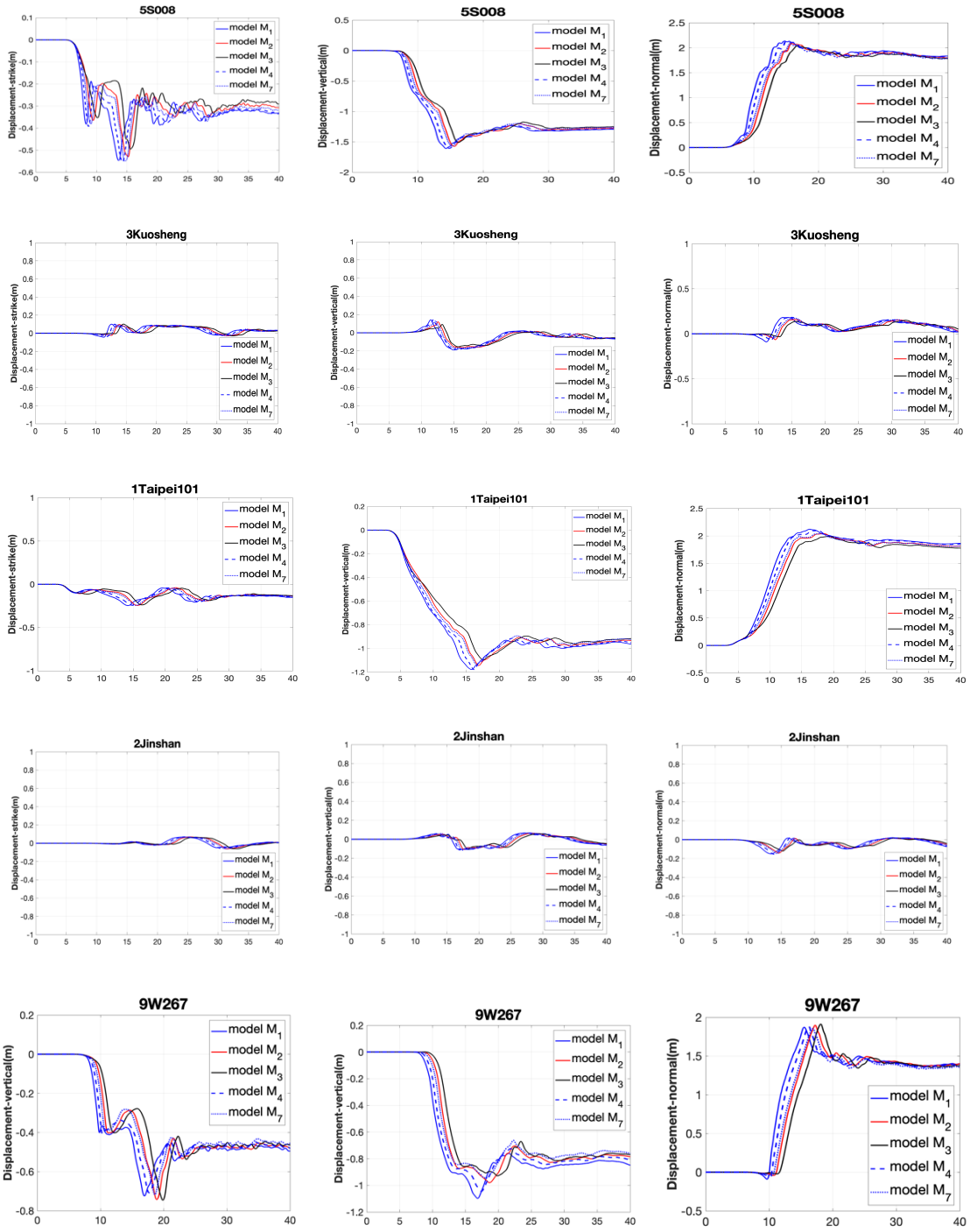

Figure 4.23. Simulated particle displacement history on the off-fault stations 1Taipei101, 2Jinshan, 3Kuosheng, 5S008, and 9W267 from P-alert network. The x-axis is the time (sec), and the y-axis is the peak ground velocity (m/s). Five models are plotted as in the figures.

The peak ground velocity and displacement of five stations, 1Taipei101, 2Jinshan, 3Kuosheng, 5S008, and 9W267, for five models M_1, M_2, M_3, M_4, and M_7 are shown in Figure 4.22 and Figure 4.23, respectively. The five models are chosen in the order of decreasing R values and increasing μ_s values. Comparing M_1, M_2 and M_3, the arrival times of the waves are delayed for decreasing R values. The model of M_1 has the largest PGV and M_3 has the smallest PGV. Comparing M_1, M_4 and M_7, the arrival time of the wave are delayed for increasing μ_s **,** i.e., S values. In conclusion, the model of M_1 has the largest PGV while the model of M_7 has the smallest.

4.4. What We Learnt: A Broader View

There are a number of basins in Taiwan [Yu et al., 1996; Lin et al., 2009; Sibuet et al., 1997] that can play an important role in seismic hazard. The ground motion could be significantly affected by the surface waves generated by the basins. Basin effects would contribute to the amplification of the PGAs and PGVs to the sites within or on the edge of the basin. The shape of the basin could affect the ground motion, too. Our results also show that the rupture propagation may be facilitated by bend fault geometry in a normal fault system. These results can have important implications to seismic hazard assessment of other regions with sedimentary basins and complex fault geometry worldwide.

4.5. Conclusion

In this study, we simulate dynamic ruptures and ground motions induced by scenario earthquakes on Chinshan-Shanqiao fault and the nearby Taipei low-velocity basin. 3D realistic velocity structure is incorporated. We build a reference model M_R with homogeneous material properties and realistic fault geometries. We simulate M_0 with no kink along strike but realistic 3D velocity structure. Then, we model nine models M_1 to M_9 with both realistic fault geometries and realistic 3D velocity structures to explore how fault geometric complexity and the Taipei basin affect the rupture dynamics and ground motion. Comparing the reference model M_R and the other models, the existence of the Taipei basin amplifies the PGA and PGVs and make ruptures to propagate preferably southeastwards due to the low rigidity of the southwest portion on the fault. For near-fault PGAs, they are large in southeast portion. For PGAs at stations off the fault, Stations 5S008 and 9W267 show basin-induced amplification. The waveforms are prolongated for these stations in the basin. However, the PGAs east of the basin are relatively smaller, like at Station 1Taipei101. This effect seems to be related to the shape of the basin because the depth in the west is around 720 m and it decreases as the basin extends to the east.

We simulate nine models M_1~M_9 with different ratios between the maximum vertical principal stress and the minimum horizontal principal stress as 3.5, 3, 2.5, and different μ_s as 0.25, 0.3, 0.35, to explore how rupture propagation and ground motion would be affected by these factors. To examine how the initial stress field and S value would affect the rupture propagation and ground motion, these parameters are gradually

adjusted. With other parameters fixed, as the R value decreases or the S value increases, it takes longer for the rupture to propagate to the same on-fault location. The model M_1, which has the largest R value and smallest S value, is preferable for rupture propagation and its magnitude of peak ground velocity and displacement are larger than those of other models.

5. SUMMARY AND CONCLUSION

Dynamic ruptures of the 2016 Meinong earthquake and potential ground motion induced by earthquake scenarios on the geometrically complex Chinshan-Shanqiao faults in Taiwan have been modeled. Realistic 3D velocity structures have been incorporated to evaluate the ground motion for Chinshan-Shanqiao fault.

We first simulate dynamic ruptures from the Meinong earthquake in southwest Taiwan. We reproduce slip distribution, rupture process and moment rate history from kinematic inversions to understand the mechanics that causes the complex rupture details. The Meinong earthquake occurs on a buried and shallow dipping fault with dominant left-lateral strike slip with limited amount of thrusting. By try-and-error, we find in our best fit model two asperities with sizes of 15 by 8 km along strike and dip and of 10 by 6 km dominate the moment release. The average stress drops in the two asperities are 5 and 3.5 MPa, respectively. The whole rupture region is 25 by 25 km. Except for asperities, the region near the hypocenter has a very low 0.75 MPa stress drop. The magnitude of the best model is M_w 6.63 and the maximum slip is 1.40 m, close to M_w 6.52 and 1.2 m from inversions. We apply a uniform velocity structure to simulate ground motions and find the simulated peak ground velocities match the seismograms on rock sites in 0-0.5 Hz. Inside low-velocity sedimentary Tainan basin, simulated peak ground velocities also match the recorded vertical peak ground velocities. However, the horizontal peak ground velocities are less than those from records. Therefore, we conclude that the uniform velocity

structure works well for the rock sites but 3D velocity structure is important to generate the large horizontal ground motions recorded in the Tainan basin during the earthquake.

In the second study, we simulate dynamic ruptures and ground motions induced by scenario earthquakes on Chinshan-Shanqiao fault and the nearby Taipei low-velocity basin. 3D realistic velocity structure is incorporated. We build a reference model M_R with homogeneous material properties and realistic fault geometries. We simulate M_0 with no kink along strike but realistic 3D velocity structure. Then, we model nine models M_1 to M_9 with both realistic fault geometries and realistic 3D velocity structures to explore how fault geometric complexity and the Taipei basin affect the rupture dynamics and ground motion. Comparing the reference model M_R and the other models, the existence of the Taipei basin amplifies the PGA and PGVs. For near-fault PGAs, they are large in southeast portion. For PGAs at stations off the fault, Stations 5S008 and 9W267 show basin-induced amplification. The waveforms are prolongated for these stations in the basin. However, the PGAs east of the basin are relatively smaller, like at Station 1Taipei101. This effect seems to be related to the shape of the basin because the depth in the west is around 720 m and it decreases as the basin extends to the east. In terms of rupture dynamics, the R value decrease or the S value increase make it longer for the rupture to propagate to the same on-fault location.

REFERENCES

Andrews, D. J. (1976a), Rupture propagation with finite stress in antiplane strain, J. Geophys. Res., 81, 3575-3582.

Andrews, D. J. (1976b), Rupture velocity of plane strain shear cracks, J. Geophys. Res., 81, 5679-5687.

Aochi H, E. Fukuyama (2002), Three-dimensional nonplanar simulation of the 1992 Landers earthquake, Journal of Geophysical Research, Vol. 107, No. B2, 2035, 10.1029/2000JB000061

Aochi H., R., Madariaga (2003), Bulletin of the Seismological Society of America 93 (3), 1249-1266

Aochi, H., O. Scotti, and C. Berge-Thierry (2005), Dynamic transfer of rupture across differently oriented segments in a complex 3-D fault system, Geophys. Res. Lett., 32, L21304, doi:10.1029/2005GL024158.

Berenger J.-P (1994), A perfectly matched layer for the absorption of electromagnetic waves, Journal of Computational Physics,Volume 114, Issue 2 ,Pages 185-200

Bos, A. G., W. Spakman, and M. C. J. Nyst (2003), Surface deformation and tectonic setting of Taiwan inferred from a GPS velocity field, J. Geophys. Res., 108(B10), 2458, doi:10.1029/2002JB002336.

Brocher, T. (2005), Empirical relations between elastic wavespeeds and density in the Earth's crust. Bull. Seismol. Soc. Am. **95**, 2081–2092. doi:10.1785/0120050077

Chai, B. H. T. (1972), Structure and tectonic evolution of Taiwan: American Journal of Science, v. 272, p. 389–422.

Chang, H.-C., C.-W. Lin, M.-M. Chen, and S.-T. Lu (1998), An introduction to the active faults of Taiwan, explanatory text of the active fault map of Taiwan, Special Publication of Central Geological Survey, 10, 1–103.

Chang, W.-L., K.-E. Ching, C.-H. Lee, Y.-R. Lee, and C.-F. Lee (2016), Earthquake Potential of Active Faults in Taiwan from GPS Observations and Block Modeling, Seismological Research Letters Volume 87, doi: 10.1785/022016009

Chen, C. T., J. C. Lee, Y. C. Chan, and C. Y. Lu (2010): Growth normal faulting at the western edge of the Metropolitan Taipei Basin since the last glacial maximum, northern Taiwan. Terr. Atmos. Ocean. Sci., 21, 409-428 (TH)

Chen, C.-T., J.-C. Lee, Y.-C. Chan, C.-Y. Lu, and L. S.-Y. Teng (2014), Elucidating the geometry of the active Shanchiao Fault in the Taipei metropolis, northern Taiwan, and the reactivation relation- ship with preexisting orogen structures, Tectonics, 33, 2400–2418, doi:10.1002/ 2013TC003502.

Collino F. and Tsogka C. (2001) Application of the perfectly matched absorbing layer model to the linear elastodynamic problem in anisotropic heterogeneous media. Geophysics, 66:1, 294-307

Das, S., and K. Aki (1977), A numerical study of two-dimensional spontaneous rupture propagation, Geophys. J. Roy. Astron. Soc., 50, 643-668.

Das, S., J. Boatwright, C.H. Scholz (Eds.) (1986), Earthquake Source Mechanics, Am. Geophys., Union. M. Ewing Vol. 6, Geophys. Monogr., 37, pp. 25-35

Davies, J.H., and von Blanckenburg, F. (1995), Slab breakoff: A model of lithosphere detachment and its test in the magmatism and deformation of collisional orogens. Earth Planet. Sci. Lett. 129, 85

Day, S. M., L. A. Dalguer, N. Lapusta, and Y. Liu (2005), Comparison of finite difference and boundary integral solutions to three-dimensional spontaneous rupture, J. Geophys. Res., 110, B12307, doi:10.1029/2005JB003813.

Day, S. M.; Three-dimensional simulation of spontaneous rupture: The effect of nonuniform prestress. Bulletin of the Seismological Society of America ; 72 (6A): 1881–1902.

Diao H.-Q, H. Kobayashi, and K. Koketsu (2018), Rupture Process of the 2016 Meinong, Taiwan, Earthquake and Its Effects on Strong Ground Motions, Bulletin of the Seismological Society of America, Vol. 108, No. 1, pp. 163–174, February 2018, doi: 10.1785/0120170193

Duan, B. (2008a), Effects of low-velocity fault zones on dynamic ruptures with nonelastic off-fault response, Geophys. Res. Lett., 35, L04307, doi:10.1029/2008GL033171.

Duan, B. (2008b), Asymmetric off-fault damage generated by bilateral ruptures along a bimaterial interface, Geophy. Res. Lett., 35, L14306, doi:10.1029/2008GL034797.

Duan, B. (2010a), Role of initial stress rotations in rupture dynamics and ground motion: A case study with implications for the Wenchuan earthquake, J. Geophys. Res., 115, B05301, doi:10.1029/2009JB006750.

Duan, B. (2010b), Inelastic response of compliant fault zones to nearby earthquakes, Geophys. Res. Lett., L16303, doi:10.1029/2010GL044150.

Duan, B. (2012), Dynamic rupture of the 2011 Mw 9.0 Tohoku-Oki earthquake: Roles of a possible subducting seamount, J. Geophys. Res., 117, B05311

Duan, B. (2012), Dynamic rupture of the 2011 Mw 9.0 Tohoku-Oki earthquake: Roles of a possible subducting seamount, J. Geophys. Res., 117, B05311, doi:10.1029/2011JB009124.

Duan, B., and D. D. Oglesby (2005), Multicycle dynamics of nonplanar strike-slip faults, J. Geophys. Res., 110, B03304, doi:10.1029/2004JB003298.

Duan, B., and D. D. Oglesby (2007), Nonuniform prestress from prior earthquakes and the effect on dynamics of branched fault systems, J. Geophys. Res., 112, B05308, doi:10.1029/2006JB004443.

Duan, B., and Oglesby, D. D. (2006), Heterogeneous fault stresses from previous earthquakes and the effect on dynamics of parallel strike-slip faults, J. Geophys. Res., 111, B05309, doi:10.1029/2005JB004138.

Duan, B., and S. M. Day (2008), Inelastic strain distribution and seismic radiation from rupture of a fault kink, J. Geophys. Res., 113, B12311, doi:10.1029/2008JB005847.

Duan, B., D. Liu, and A. Yin (2017), Seismic shaking in the North China Basin expected from ruptures of a possible seismic gap, Geophys. Res. Lett., 44, 4855–4862, doi:10.1002/ 2017GL072638.

Festa, G., and S. Nielsen (2003). PML absorbing boundaries, Bull. Seismol. Soc. Am. 93 891-903.

Guatteri, M., and P. Spudich (2000), What can strong motion data tell us about slip-weakening fault-friction laws?, Bull. Seism. Soc. Am. 90, 98–116.

Harris, R. A. and Barall, M. and Archuleta, R. and Dunham, E. and Aagaard, B. T. and Ampuero, J. P. and Bhat, H. and Cruz-Atienza, V. and Dalguer, L. and Dawson, P. and Day, S. and Duan, B., B. and Ely, G. and Kaneko, Y. and Kase, Y. and Lapusta, N. and Liu, Y. and Ma, S. and Oglesby, D. and Olsen, K. and Pitarka, A. and Song, S. and Templeton, E. (2009), The SCEC/USGS Dynamic Earthquake Rupture Code Verification Exercise. Seismological Research Letters, 80 (1). pp. 119-126. ISSN 0895-0695.

Harris, R. A., Barall, M., Aagaard, B., Ma, S., Roten, D., Olsen, K., Duan, B., Luo, B., Liu, D., Bai, K., Ampuero, J., Kaneko, Y., Gabriel, A., Duru, K., Ulrich, T., Wollherr, S., Shi, Z., Dunham, E., Bydlon, S., Zhang, Z., Chen, X., Somala, S., Pelties, C., Tago, J., Cruz-Atienza, V., Kozdon, J., Daub, E., Aslam, K., Kase, Y., Withers, K., & Dalguer, L. (2018), A suite of exercises for verifying dynamic earthquake rupture codes. Seismological Research Letters, 89(3), 1146-1162. doi: 10.1785/0220170222. SCEC Contribution 7960

Hough, S.E., P. A. Friberg, R. Busby, E. F. Field, K. H. Jacob & R. D. Borcherdt (1990), Sediment-induced amplification and the collapse of the Nimitz Freeway , Nature volume 344, pages853–855. DOI https://doi.org/10.1038/344853a0

Hsu, M.T. (1971), Seismicity of Taiwan and some related problems. Bulletin of the International Institute of Seismology and Earthquake Engineering 8, 41–160.

Huang, H.H., Wu, Y.M., Song, X.D., Chang, C.H., Lee, S.J., Chang, T.M., Hsieh, H.H. (2014), Joint Vp and Vs tomography of Taiwan: Implications for subduction-collision orogeny. Earth Planet. Sci. Lett. 392, 177-191https://doi.org/10.1016/j.epsl.2014.02.026

Huang, M.-H., H. Tung, E. J. Fielding, H.-H. Huang, C. Liang, C. Huang, and J.-C. Hu (2016), Multiple fault slip triggered above the 2016 Mw 6.4 MeiNong earthquake in Taiwan, Geophys. Res. Lett., 43, 7459–7467, doi:10.1002/ 2016GL069351.

Huang, S.-Y., C. M. Rubin, Y.-G. Chen, Huan-Chi Liu (2007), Prehistoric earthquakes along the Shanchiao fault, Taipei Basin, northern Taiwan, Journal of Asian Earth Sciences 31 265–276

Ida, Y., and Aki, K. (1972), Seismic source time function of propagating longitudinal-shear cracks, J. Geophys. Res., 77(11), 2034– 2044, doi:10.1029/JB077i011p02034.

Irikura, K., and H. Miyake (2010), Recipe for predicting strong ground motion from crustal earthquake scenarios, Pure Appl. Geophys., doi:10.1007/s00024-010-0150-9.

Jian, P.-R., Hung, S.-H., Meng, L., and Sun, D. (2017), Rupture characteristics of the 2016 Meinong earthquake revealed by the back projection and directivity analysis of teleseismic broadband waveforms, Geophys. Res. Lett., 44, 3545– 3553, doi:10.1002/2017GL072552.

Kosloff, D. and Frazier, G. A. (1978), Treatment of hourglass patterns in low order finite element codes. Int. J. Numer. Anal. Meth. Geomech., 2: 57-72. doi:10.1002/nag.1610020105

Kuo, C., H., F. T. Wu, and S. W. Roecker (2012), Three-Dimensional P Velocity Structures of the Lithosphere Beneath Taiwan from the Analysis of TAIGER and Related Seismic Data sets, J. Geophys. Res., 117, B06306, doi:10.1029/2011JB009108.

Kuo, C., H., Wu, F.T., Roecker, S.W. (2012), Three-dimensional P velocity structures of the lithosphere beneath Taiwan from the analysis of TAIGER and related seismic data sets. J. Geophys. Res. 117, B06306. 10.1029/2011JB009108

Lai, J. S., C. Y. Chiu, H. K. Chang, J. C. Hu, and Y. C. Tan (2010), Potential inundation hazards in the Taipei Basin induced by reactivation of the Shanchiao fault in northern Taiwan. Terr. Atmos. Ocean. Sci., 21, 529-542, doi: 10.3319/TAO.2010.02.22.01(TH)

Lee, S. J., H. W. Chen, Q. Liu, D. Komatitsch, B. S. Huang, and J. Tromp (2008). Three-dimensional simulations of seismic wave propagation in the Taipei basin with realistic topography based upon the spectral element method, Bull. Seismol. Soc. Am. 98, 253–264, doi 10.1785/ 0120070033.

Lee, S.-J., T.-Y. Yeh and Y.-Y. Lin (2016), Anomalously Large Ground Motion in the 2016 ML 6.6 Meinong, Taiwan, Earthquake: A Synergy Effect of Source Rupture and Site Amplification, Seismological Research Letters, 87 (6), doi: 10.1785/0220160082

Lee Y. T. Wang Y. J. Chan C. H., and Ma K. F. (2017), The 2016 Meinong earthquake to TEM PSHA2015, Terr. Atmos. Ocean. Sci. 28, 703–713, doi: https://doi.org/10.3319/TAO.2016.12.28.02.

Lin, C.W., H.C. Chang, S.T. Lu,T.S. Shih,a ndW.J. Huang (2000), An Introduction to the Active Faults of Taiwan, 2nd Ed., Explanatory Text of the Active Fault Map of Taiwan. Spec. Publ. Cent. Geol. Surv., 13, 122 pp. (in Chinese)

Lin, C.W., S.T. Lu, and W. S., Chen (2012), Active Fault Map of Taiwan: An Explanatory Text. Spec. Publ. Cent. Geol. Surv., 26, 1-30. (in Chinese)

Lin, D.-H, K. Chen, R.-J Rau, J.-C Hu (2013),The role of a hidden fault in stress triggering: Stress interactions within the 1935 Mw 7.1 Hsinchu–Taichung earthquake sequence in central Taiwan, Tectonophysics, Volume 601, Pages 37-52

Lin, Z., T. Oguchi, Y.-G. Chen, K. Saito (2009), Constant-slope alluvial fans and source basins in Taiwan, Geology, 37 (9): 787–790. doi: https://doi.org/10.1130/G25675A.1

Liu, D., B. Duan (2018), Scenario Earthquake and Ground-Motion Simulations in North China: Effects of Heterogeneous Fault Stress and 3D Basin Structure. Bulletin of the Seismological Society of America ; 108 (4): 2148–2169. doi: https://doi.org/10.1785/0120170374

Ma, S., and P. C. Liu (2006). Modeling of the perfectly matched layer absorbing boundaries and intrinsic attenuation in explicit finite-element methods, Bull. Seismol. Soc. Am. 96 1779-1794.

McCaffrey, R., Molnar, P., Roecker, S., and Joyodiwiryo, Y. (1985), Microearthquake seismicity and fault plane solutions related to arc-continent collision in the eastern Sunda arc, Indonesia: Journal of Geophysical Research , v. v. 90pp. 4511452□

McCalpin, J.P., Nishenko, S.P. (1996), Holocene paleoseismicity, temporal clustering, and probabilities of future large (M > 7) earthquakes on the Wasatch fault zone, Utah. Journal of Geophysical Research 101 (B3), 6233–6253.

Oglesby, D. D. (2008). Rupture termination and jump on parallel offset faults. Bulletin of the Seismological Society of America, 98(1), 440-447. https://doi.org/10.1785/0120070163

Okubo, P. G. and Dieterich, J. H. (2013). State Variable Fault Constitutive Relations for Dynamic Slip. In Earthquake Source Mechanics (eds S. Das, J. Boatwright and C. H. Scholz). doi:10.1029/GM037p0025

Okubo, P. G. (1989), Dynamic rupture modeling with laboratory-derived constitutive relations, J. Geophys. Res., 94(B9), 12321– 12335, doi:10.1029/JB094iB09p12321.

Okubo, P. G. and Dieterich, J. H. (2013). State Variable Fault Constitutive Relations for Dynamic Slip. In Earthquake Source Mechanics (eds S. Das, J. Boatwright and C. H. Scholz). doi:10.1029/GM037p0025

Olsen, K. B., S. M. Day, C. R. Bradley (2003), Estimation of Q for Long-Period (>2 sec) Waves in the Los Angeles Basin. Bulletin of the Seismological Society of America ; 93 (2): 627–638. doi: https://doi.org/10.1785/0120020135

Olsen, K. B., Day, S. M., Minster, J. B., Cui, Y., Chourasia, A., Faerman, M., Moore, R., Maechling, P., and Jordan, T. (2006), Strong shaking in Los Angeles expected from southern San Andreas earthquake, Geophys. Res. Lett., 33, L07305, doi:10.1029/2005GL025472.

Olsen, K. B., S. M. Day, J. B. Minster, Y. Cui, A. Chourasia, D. Okaya, P. Maechling, T. Jordan (2008), TeraShake2: Spontaneous Rupture Simulations of Mw 7.7 Earthquakes on the Southern San Andreas Fault. Bulletin of the Seismological Society of America ; 98 (3): 1162–1185. doi: https://doi.org/10.1785/0120070148

Olsen, K. B., et al. (2009), ShakeOut-D: Ground motion estimates using an ensemble of large earthquakes on the southern San Andreas fault with spontaneous rupture propagation, Geophys. Res. Lett., 36, L04303, doi:10.1029/2008GL036832.

Schwartz, D.P., Coppersmith, K.J. (1984), Fault behavior and characteristic earthquakes; examples from the Wasatch and San Andreas fault zones. Journal of Geophysical Research 89 (B7), 5681–5698.

Sekiguchi, H., K. Irikura, T. Iwata, Y. Kakehi, and M. Hoshiba (1996), Minute locating of faulting beneath Kobe and the waveform inversion of the source process during the 1995 Hyogo-ken Nanbu, Japan, earthquake using strong ground motion records, J. Phys. Earth, 44, 473 – 487.

Shin, T.-Z., T.-L. Teng (2001), An Overview of the 1999 Chi-Chi, Taiwan, Earthquake. Bulletin of the Seismological Society of America ; 91 (5): 895–913. doi: https://doi.org/10.1785/0120000738

Sibuet, J.-C, S.-K Hsu (1997), Geodynamics of the Taiwan arc-arc collision, Tectonophysics, Volume 274, Issues 1–3, Pages 221-251

Teng, L.S., C.-T. Lee (1996), Geodynamic appraisal of seismogenic faults in northeast Taiwan Geological Society of China, 39, pp. 125-142

Teng, L.S. (1996), Extensional collapse of the northern Taiwan mountain belt. Geology ; 24 (10): 949–952.

Teng, L.S., C. T. Lee, Y. B. Tsai, Li-Yuan Hsiao (2000), Slab breakoff as a mechanism for flipping of subduction polarity in Taiwan. Geology ; 28 (2): 155–158.

Thomas J. R. Hughes (2000), The Finite Element Method: Linear Static and Dynamic Finite Element Analysis,

Tsai, C.-M, W.-J Huang, P.-C Chan and S.-T Lu (2014), Topographic change and potential inundation hazard in the Greater Taipei area and Coulomb stress on neighboring faults induced by the reactivation of the Shanchiao fault in northern Taiwan, CGS Bulletin (in Chinese)

Tsai YB (1986), Seismotectonics of Taiwan, Tectonophysics 125:17-38

Wang, J. H.(2008), Potential earthquakes rupturing the Chinshan and Shangjiao faults in the Taipei Metropolitan Area. Terr. Atmos. Ocean. Sci., 19, 205-212, doi: 10.3319/TAO.2008.19.3.205(T)

Wang, J., Chen, K., Lee, S., & Huang, W. (2011), The 15 April 1909 Taipei Earthquake.

Wang YM, Lee SJ, Ng SM (2012), "The Big One" in Taipei: numerical simulation study of the Sanchiao Fault earthquake scenarios. American Geophysical Union, Fall Meeting

Wang JP, Kuo-Chen H (2015), On the use of AFOSM to estimate major earthquake probabilities in Taiwan. Nat Hazards 75:2577–2587

Wang J.P. , M.-H Wu (2015)，Risk assessments on active faults in Taiwan，Bull Eng Geol Environ 74:117–124 doi: 10.1007/s10064-014-0600-1

Wortel, M.J.R., and Spakman, W. (1992), Structure and dynamics of subducted lithosphere in the Mediterranean region, *Proc. K. Ned. Akad. Wet.*, **95**, 325–347.

Wu, Y. M., D. Y. Chen, T. L. Lin, C. Y. Hsieh, T. L. Chin, W. Y. Chang, W. S. Li, and S. H. Ker (2013), A highdensity seismic network for earthquake early warning in Taiwan based on low cost sensors. Seismol. Res. Lett., 84, 1048-1054

Xu, Y. and P. Wang, J. (2017), Earthquake recurrence assessment of the active Shanchiao Fault in northern Taiwan. Natural Hazards. 88. 10.1007/s11069-017-2894-3.

Yoshida, S., K. Koketsu, B. Shibazaki, T. Sagiya, T. Kato, and Y. Yoshida (1996), Joint inversion of near- and far-field waveforms and geodetic data for the rupture process of the 1995 Kobe earthquake, J. Phys. Earth, 44, 437 – 454.

Yu H.-S, J. Chow (1997), Cenozoic basins in northern Taiwan and tectonic implications for the development of the eastern Asian continental margin,Palaeogeography, Palaeoclimatology, Palaeoecology, Volume 131, Issues 1–2,Pages 133-144

Yu, S.-B., H. Y. Chen, and L. C. Kuo (1997), Velocity field of GPS stations in the Taiwan area, Tectonophysics, 274, 41 – 59.

Yu, S.-B. and L.-C. Kuo, R. S. Punongbayan and E. G. Ramos (1999), GPS observation of crustal deformation in the Taiwan-Luzon Region, Geophysical Research Letters, Vol. 26, No. 7, Pages 923-926